ARTICLE | Article in Press

Amine-functionalized cobalt ferrite nanoparticles as efficient magnetically separable adsorbents for Pb(II) and *E. coli*

Dóra Tergalecz · Orsolya Alberti · Maria Ilosvai · Ferenc Kristály · Lajos Daróczi · Béla Viskolcz · Emma Szőri-Dorogházi · László Vanyorek · Emőke Sikora

Received: 17 March 2026 / Accepted: 14 September 2026

Abstract

Amine-functionalized cobalt ferrite ($CoFe_2O_4$–NH_2) nanoparticles were synthesized via a polyol-based solvothermal route and compared with non-functionalized $CoFe_2O_4$ prepared by a sonochemical–combustion method as magnetically separable adsorbents. Structural and physicochemical properties were characterized by HRTEM, SAED, XRD, FTIR, VSM, N_2 and CO_2 adsorption. The functionalized material formed porous spherical aggregates (51 ± 8 nm) composed of 4–8 nm crystallites, exhibiting a significantly enhanced specific surface area compared to pristine $CoFe_2O_4$. Both samples displayed ferrimagnetic behaviour with high saturation magnetization, enabling rapid magnetic separation. Adsorption studies toward Pb(II), Cd(II), and Ni(II) revealed strongly ion-dependent behaviour. Langmuir modelling yielded a maximum adsorption capacity of 86.4 ± 1.5 mg g^{-1} for Pb(II) on $CoFe_2O_4$–NH_2, more than twice that of the non-functionalized analogue. Furthermore, $CoFe_2O_4$–NH_2 achieved complete removal (100%) of *Escherichia coli* (10^2 cfu/mL) at 3–30 mg/mL and retained full efficiency after five reuse cycles. The results demonstrate that amine functionalization markedly enhances adsorption performance while preserving magnetic separability, highlighting the potential of $CoFe_2O_4$–NH_2 as a multifunctional platform for water remediation.

Keywords Toxic metals · Bacteria · Magnetic · Ferrite · Amine functionalized · Adsorption

Introduction

Rapid industrialization and significant industrial wastewater discharges have transformed the aquatic ecosystem. The demand for a sustainable water supply is increasing in today's world, which necessitates the rapid and efficient removal of pollutants from the aquatic environment.

As the discussion of water pollutants becomes increasingly important, the terminology used to describe these contaminants also requires careful consideration. Several authors have also pointed out that the widely used term "heavy metals" is scientifically imprecise and inconsistently defined. Duffus[1] and later Hübner et al.[2] therefore recommended the use of more accurate terminology, such as "toxic metals" or "potentially toxic metals",

Published online: 17 September 2026

depending on the environmental context and chemical behavior of the elements involved. In accordance with these recommendations, the present study uses the term "toxic metals" throughout the manuscript.

Magnetic nanoadsorbents offer the advantage of easy magnetic separation[3]. Ferrites are ferrimagnetic compounds primarily composed of iron oxides (Fe_2O_3 and FeO), in which iron ions can be partially substituted by other transition metal ions[4,5]. Ferrite nanoparticles are mainly produced by wet chemical ssol–gell or coprecipitation methods, less commonly by sonochemical techniques, high-energy mechanical ball milling, spark-plasma sintering, microwave heating, or hydrothermal methods. Nanoparticles in the superparamagnetic state can be of key importance in water purification. In the absence of an external magnetic field, the nanoparticles do not agglomerate and do not retain residual magnetism, which allows them to be easily dispersed in water[6].

The properties of ferrites are largely governed by how cations are distributed among the lattice sites, and doping has the strongest impact on this distribution. When foreign metal ions enter the structure, they occupy sites according to their preference, thereby altering the structural, magnetic, electrical, and catalytic behavior of cobalt ferrite[7]. Between the spinel forms of ferrites, cobalt ferrite ($CoFe_2O_4$) is a well-known and studied form due to its mechanical hardness, moderate saturation magnetization, high coercive force and chemical stability[8,9–11]. Although cobalt-containing ferrites are less attractive for large-scale applications due to sustainability and raw-material considerations, $CoFe_2O_4$ remains an important model system for studying magnetic adsorbents.

Several research groups have focused on the synthesis of different spinel ferrite nanoparticles and their application as adsorbents for wastewater treatment[12–21]. W. A. Khoso and colleagues synthesized magnetic nickel ferrite nanoparticles (NFNs) using a co-precipitation method and applied them for the removal of Cr(VI), Pb(II) and Cd(II). The removal efficiencies under optimal conditions were 89%, 79% and 87%, respectively[22]. Z. Iqbal and his team produced reduced graphene oxide-modified spinel cobalt ferrite nanoparticles (RGCF)[23]. M. Irfan and his group prepared amine-functionalized magnesium ferrite ($MgFe_2O_4$) nanoparticles using a sol–gel route and calcined them at different temperatures. The sample calcined at 500 °C showed the best performance, removing Pb(II) (0.715 mmol/g, 73%), Cu(II) (0.657 mmol/g, 59%) and Zn(II) (0.768 mmol/g, 62%)[14]. M. A. Ahmed synthesized reduced graphene oxide by a modified Hummers method and decorated it with zinc ferrite nanoparticles for the removal of Pb(II) and methylene blue. The material showed adsorption capacities of 89.9 mg/g for Pb(II) and 119.0 mg/g for methylene blue and could be reused for at least five cycles[24]. R. Ramadan doped $CoFe_2O_4$ with Zn and Co using a flash auto-combustion method and tested the materials for Cr(VI) removal. The best results were obtained for Co-$CoFe_2O_4$ (93%) and Zn-$CoFe_2O_4$ (90%)[25]. R. Jayalakshmi's group studied cobalt ferrite nanoparticles synthesized by co-precipitation and applied them to remove Pb(II), Zn(II), Congo Red (CR) and Malachite Green (MG), reaching maximum removal capacities of 275 mg/g (96%) for Pb, 390 mg/g (92%) for Zn, 831 mg/g (99%) for CR and 161 mg/g (92.5%) for MG[26]. E. C. Paris and her colleagues synthesized faujasite zeolite by sol–gel and decorated it with cobalt ferrite, achieving an adsorption capacity of 602.4 mg/g for Pb(II) according to the Langmuir model[20]. N. S. Asri used $CoFe_2O_4$ nanoparticles prepared by co-precipitation to remove Cu(II), Fe(II) and Ni(II). The addition of PEG-4000 as a coating agent decreased the adsorption efficiency, but without it, removal efficiencies of around 98% were obtained[19]. X. Zhao and co-workers doped cobalt ferrite nanoparticles with gadolinium, achieving a maximum adsorption capacity of 263.2 mg/g at an optimal atomic ratio of $x = 0.07$[27]. Z. Ding synthesized $CoFe_2O_4$ nanoparticles via an ethanol-assisted hydrothermal route for Congo Red removal, with a maximum capacity of 190.5 mg/g[28]. Further work by M. U. Saleem demonstrated that functionalized $CoFe_2O_4$ nanoparticles coated with silica and modified with amine groups had improved adsorption compared to pristine $CoFe_2O_4$, reaching 277.0, 254.5 and 258.4 mg/g for Cu(II), Pb(II) and Zn(II), respectively[21]. K. Al Yaqoob studied MFe_2O_4 nanoparticles (M = Co, Ni, Cu, Zn) synthesized by microwave combustion for Pb(II) and Cd(II) removal. The highest adsorption was observed for Cd(II) at 157.7 mg/g using $CoFe_2O_4$, while for Pb(II) the best result was 63.1 mg/g with $CoFe_2O_4$[15].

Several studies have also investigated the applicability of magnetic nanoparticles in biological water purification, demonstrating that beyond toxic metal adsorption these materials can also remove harmful pathogenic bacteria from aqueous environments. For example, Y-F. Huang and colleagues tested amine-functionalized magnetic

nanoparticles for microorganism adsorption using an *Escherichia coli (E. coli*) strain, achieving a 93.8% removal efficiency of microbial cells from water, beverage, and urine samples with nanoparticle dispersions at a concentration of 0.5 mg/mL[29]. Similarly, R. A. Bohara and his co-workers examined amine-functionalized cobalt ferrite nanoparticles with respect to their bacteria-binding properties. At concentrations of 1 mg/mL and 2 mg/mL, the tested MNPs (magnetic nanoparticles) adsorbed 65% o *E. coli* cells after 60 min incubation[30]. A. J. Franco and colleagues investigated chitosan-coated magnetic nanoparticles with respect to their ability to adsorb *Salmonella enteritidis* and *E. coli* bacteria. Experiments performed using MNP dispersions at a concentration of 5 mg/mL demonstrated that adsorption occurred within 15 min, and in all cases the adsorption capacity was notably higher for *E. coli*[31].

Overall, these studies clearly demonstrate that spinel ferrite nanoparticles and their composites are highly effective adsorbents for the removal of toxic metal ions and bacterial cells from wastewater. By applying various synthesis routes, dopants, and surface modifications, significant improvements in adsorption efficiency, selectivity and reusability can be achieved, making them promising materials for environmental remediation. Although numerous studies have demonstrated the applicability of ferrite-based adsorbents either for toxic metal removal or for microbial adsorption, these functionalities are most often investigated separately and frequently rely on different materials or surface modification strategies. Even in the case of amine-functionalized ferrites, reports typically focus on a single target contaminant class, while a unified assessment of chemical and biological adsorption within the same material system remains limited.

In this study, the toxic metal adsorption properties of $CoFe_2O_4$ and amine-functionalized $CoFe_2O_4$ were compared, while bacterial adsorption experiments were also carried out using the functionalized material. The synthesized nanoparticles were characterized using TEM, SAED, XRD, FTIR, VSM, DLS and gas sorption measurements. The results demonstrated that amine-functionalized cobalt ferrite nanoparticles can serve as a multifunctional magnetic adsorbent, capable of efficiently removing toxic metal ions and capturing bacterial cells without further compositional modification. By directly comparing non-functionalized and amine-functionalized $CoFe_2O_4$, the present study systematically evaluates the role of amine functionalization in metal ion adsorption selectivity, reusability, and bacterial binding using the same $CoFe_2O_4$–NH_2 material. These findings highlight the potential of amine-functionalized ferrites as versatile platforms for water remediation applications.

Results and discussion

Characterization of the amine-functionalized and non-functionalized $CoFe_2O_4$ adsorbents

The nitrogen (N_2) adsorption–desorption isotherms of cobalt ferrite nanoparticles are shown in Fig. 1. The isotherms exhibit the characteristics of IUPAC type IVa isotherms, which are typical of mesoporous materials with pore diameters in the 2–50 nm range[32]. According to the results, the BET specific surface area and pore volume of the non-functionalized sample are 65.2 m^2/g and 0.17 cm^3/g, whereas for the amine-functionalized sample they are 157.4 m^2/g and 0.36 cm^3/g, respectively. Using the BJH method, the modes of the pore diameters determined from desorption results were 7.9 nm and 18.1 nm.

Pore size distribution was further evaluated using non-local density functional theory (NLDFT), which provides a more accurate description of mesoporous structures (SI Fig. 1.) than classical methods such as BJH. The DFT analysis revealed clear differences between the non-functionalized and amine-functionalized cobalt ferrite samples. For the $CoFe_2O_4$ nanoparticles, the cumulative pore volume was 0.17 cm^3/g with a mode pore diameter of approximately 11.7 nm, indicating a relatively narrow mesopore distribution. In contrast, the $CoFe_2O_4$–NH_2 sample exhibited a significantly higher pore volume of 0.35 cm^3/g and a broader pore size distribution, with a mode pore diameter of ~16 nm.

CO_2 adsorption was also applied to probe micropores that cannot be accessed by N_2 at 77 K. This measurement provides a more accurate assessment of the microporosity and complements the nitrogen-based textural analysis.

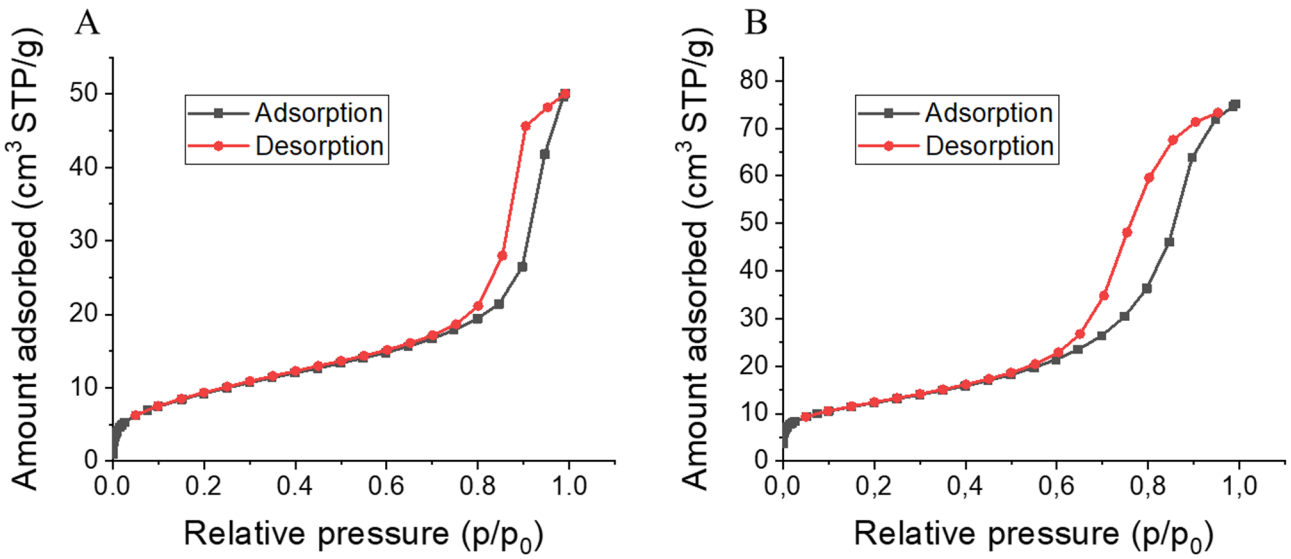

Fig. 1 Nitrogen adsorption–desorption isotherms of non-functionalized (**A**) and amine-functionalized (**B**) $CoFe_2O_4$ samples.

The specific surface area of the cobalt ferrite samples was examined also by CO_2 adsorption–desorption measurements based on the Dubinin–Astakhov method. Similar to the nitrogen adsorption measurements, a significantly higher specific surface area was determined for the amine-functionalized cobalt ferrite (279.4 m^2/g) compared to its non-functionalized counterpart (18.2 m^2/g).

These results confirm that amine functionalization and the different synthesis route promote the formation of larger interparticle mesopores and increases the overall pore volume, which is consistent with the higher BET surface area observed for this sample. The broader DFT pore size distribution correlates well with the TEM observations, where the functionalized material forms globular aggregates composed of 5–8 nm crystallites (Fig. 2A), giving rise to a hierarchical micro–mesoporous structure and increased specific surface area. The average diameter of the $CoFe_2O_4$–NH_2 particles was 51 ± 8 nm (Fig. 2B; Table 1). The "P90" and "P95" values stand for the mean diameter of 90% and 95% of the particles, respectively.

Significant differences in morphology and size distribution were observed in the case of the non-functionalized $CoFe_2O_4$ (Fig. 2D). The HRTEM images of the –NH_2 free (non-functionalized) ferrites show individual crystallites that do not form spherical aggregates, unlike the functionalized samples. The average particle diameter of the cobalt ferrite nanoparticles was 13 ± 5 nm (Fig. 2E), which differs significantly from its amine-functionalized counterpart (Table 1).

The average size of the above-detailed individual $CoFe_2O_4$ crystallites was also calculated based on X-ray diffraction measurements. The average size of the crystallites, which built up the $CoFe_2O_4$–NH_2 nanoparticles, is 4 ± 2 nm.

Selected area electron diffraction (SAED) measurements were carried out on the nanoparticles (Fig. 2C, F). Based on these measurements, d-spacing values were calculated and found to be consistent with the characteristic reflections of cobalt ferrite according to the powder diffraction files of the $CoFe_2O_4$ spinel structures. (PDF 22-1086). SAED can be used to identify individual particles but is not effective for detecting other metal oxides (cobalt oxide, hematite or magnetite) in bulk powder samples. Therefore, XRD measurements were performed to check the purity of the samples and to identify the crystalline phases of the possible contaminants (Fig. 3A and B). In both cobalt ferrite samples, reflections were identified at 18.1 ° (111), 29.9° (220), 35.3° (311), 42.5° (400), 52.7° (422), 56.3° (511) and 61.7° (440) two theta degrees (PDF 22-1086). These reflections confirm that $CoFe_2O_4$ is the only metal oxide phase present in the samples, indicating the formation of pure cobalt ferrite. This observation is valid for both samples produced by different synthesis methods.

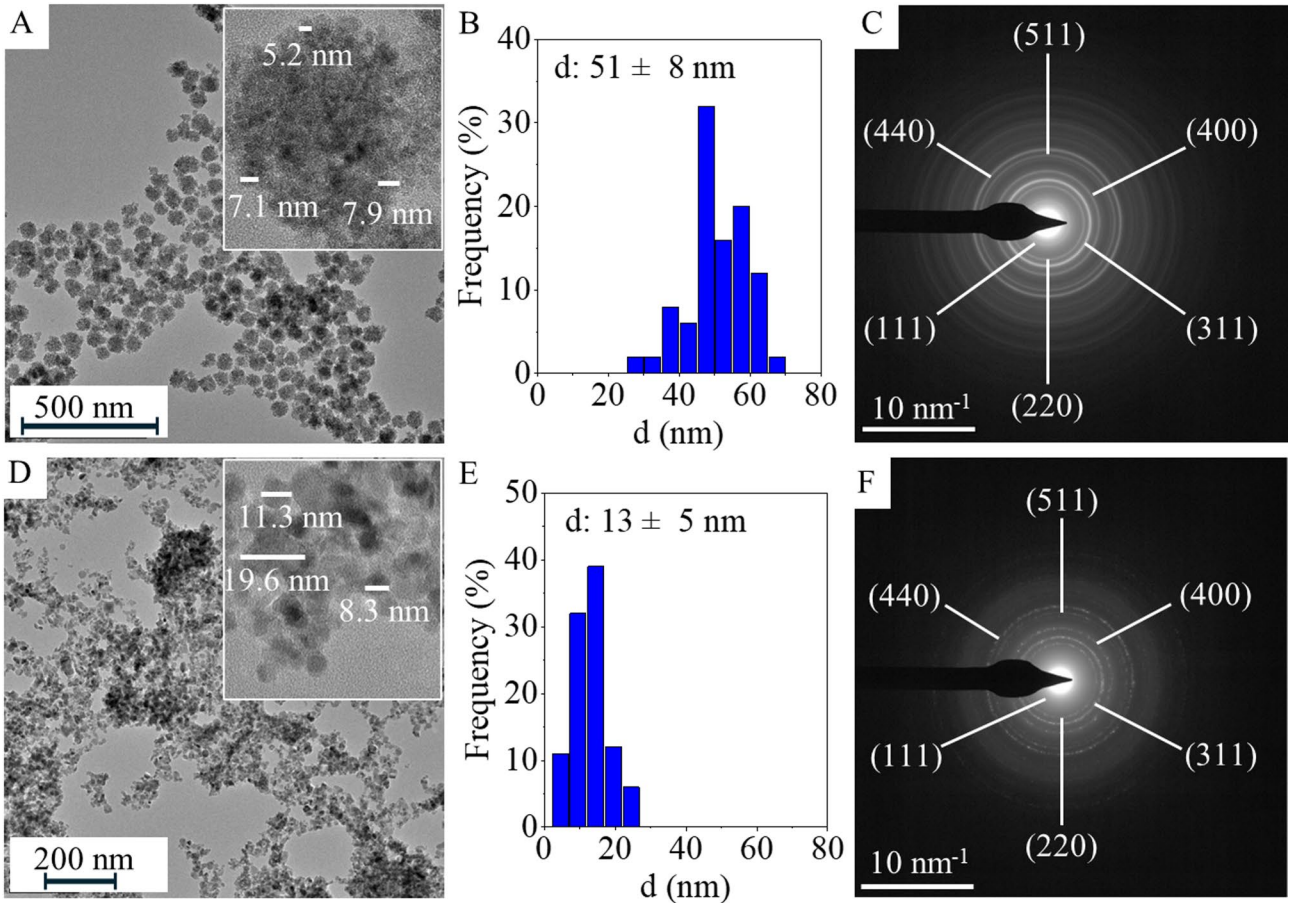

Fig. 2 HRTEM pictures, size distribution histograms and electron diffraction (selected area electron diffraction, SAED) pictures of the amine-functionalized (**A**, **B**, **C**) and non-functionalized (**D**, **E**, **F**) $CoFe_2O_4$ nanoparticles.

Table 1 Results of the size analysis (in nm) of the ferrite nanospheres of the amine-functionalized spinel samples and particles of the non-functionalized ferrites (based on HRTEM pictures).

Sample	Mean	SD	Min.	Max.	P90	P95
	Size (nm)					
$CoFe_2O_4$–NH_2	51	8	29	66	61	63
$CoFe_2O_4$	13	5	4	27	19	22

The presence of different functional groups on the surface of the ferrite nanoparticles can stongly influence their adsorption behavior, surface polarity, and dispersibility. The surface functional groups were identified by FTIR spectroscopy. The spectra of the amine-functionalized $CoFe_2O_4$ samples revealed characteristic absorption bands of surface-bound amines and hydroxyl groups (Fig. 4). In the range 1000 and 1100 cm^{-1} bands of the νC–O and the νC–N stretching vibrations are identified, which belong to the hydroxyl, carboxyl, and amino groups, respectively. Another absorption band associated with amine groups appears in the range of 1480–1740 cm^{-1} which is in convolution with the νC=C band. A broad absorption band in the 3000–3750 cm^{-1} region can be attributed to overlapping N–H and O–H stretching vibrations. Adsorbed organic molecules (ethylene glycol and monoethanolamine) were detected on the amine-functionalized cobalt ferrite ($CoFe_2O_4$–NH_2) particles, as confirmed by the presence of symmetric and asymmetric stretching vibrations of the aliphatic and aromatic C–H bonds at 2877 cm^{-1} and 2935 cm^{-1}[33]. Similar bands are also observed in the spectrum of the non-functionalized $CoFe_2O_4$ sample, because ethylene glycol was used as a reaction medium during its synthesis. Other bands

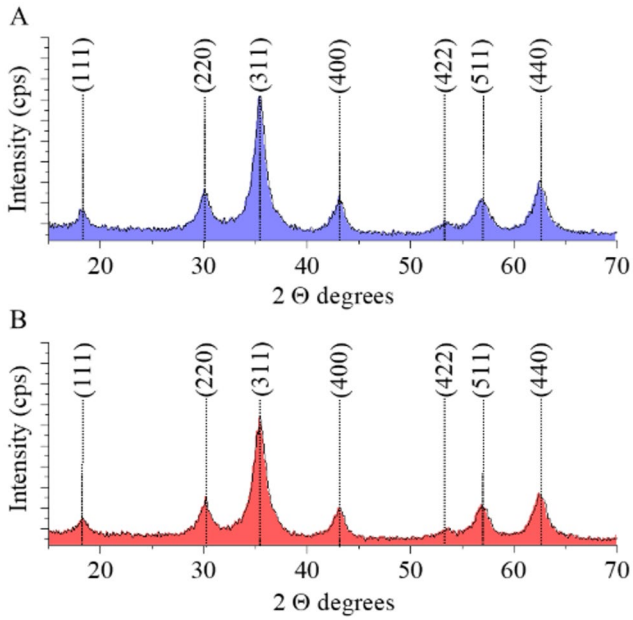

Fig. 3 X-ray diffraction (XRD) patterns of the amine-functionalized (**A**) and the non-functionalized (**B**) cobalt-ferrite.

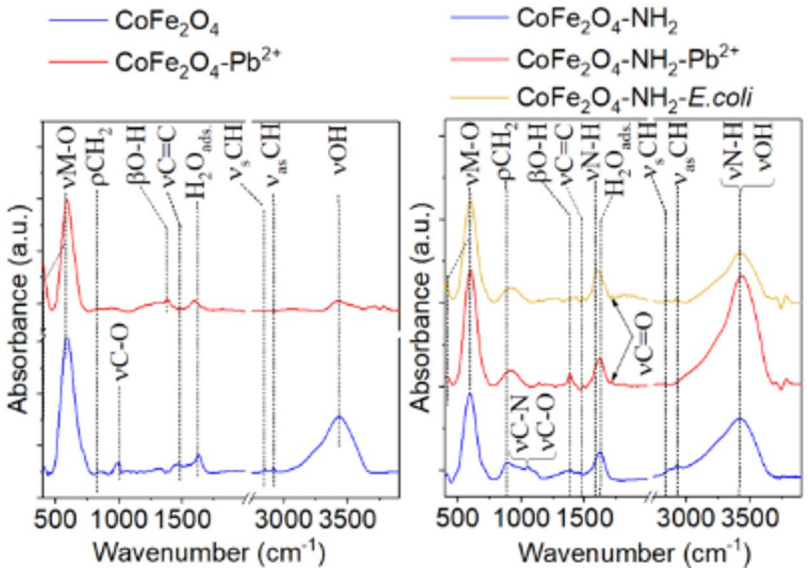

Fig. 4 FTIR spectra of the amine-functionalized and non-functionalized $CoFe_2O_4$ adsorbents before and after adsorption tests.

indicating organic residues can also be found in the $CoFe_2O_4$ spectrum at 1540 cm^{-1} and 1005 cm^{-1}; these are the bands of νC=O and νC–O vibrations. The intrinsic stretching vibration modes of the metal–oxygen bonds (νM–O) at the octahedral and tetrahedral sites in the ferrite structures of the two samples resulted in characteristic bands at 421 cm^{-1} and 596 cm^{-1} wavenumbers[34]. The band with low intensity at 1630 cm^{-1} may originate from the vibration of the adsorbed water molecules (H_2Oads). The appearance of a C=O stretching band at 1714 cm^{-1} in the FTIR spectrum of the amine-functionalized cobalt ferrite after the adsorption tests indicates the formation of carboxyl groups on the particle surface, possibly associated with oxidation of surface-bound ethylene glycol in the presence of nitrate-containing Pb(II) precursor solution. In the spectrum of the sample exposed to *E. coli* cells, a similar ν(C=O) stretching vibration appears at 1725 cm^{-1}. This band can be attributed to the carbonyl groups of nucleic acids (DNA/RNA) present in the bacterial cells, as well as to the ester linkages of membrane lipids.

CHNS analysis revealed that the carbon, hydrogen, and nitrogen contents all increased in the functionalized sample (SI Table 1.) consistent with the FTIR results. According to the CHNS elemental analysis, the nitrogen content increased from 0.04 wt% for pristine Co-ferrite to 0.85 wt% for the amine-functionalized sample.

Assuming that all nitrogen originates from surface amine functionalities, this corresponds to approximately 0.15 mol of $–NH_2$ groups per 1 mol of $CoFe_2O_4$.

The amine-functionalized and non-functionalized cobalt ferrite samples were characterized using DLS (SI Fig. 2). The pristine $CoFe_2O_4$ exhibited a strongly negative surface charge (− 25.8 ± 1.7 mV), indicating moderate colloidal stability. Upon Pb^{2+} adsorption, the zeta potential shifted to a positive value (+ 11.5 ± 1.0 mV). The amine-functionalized $CoFe_2O_4$–NH_2 showed a less negative initial charge (–13.9 ± 0.1 mV), consistent with the presence of protonatable amine groups, that can create localized positively charged interaction sites in aqueous media. After Pb^{2+} binding, its surface charge also became positive (+ 8.6 ± 2.4 mV), supporting strong interaction with lead ions. In contrast, interaction with *E. coli* cells resulted only in a moderate shift (–4.9 ± 0.3 mV).

The amine-functionalized and non-functionalized cobalt ferrite samples were characterized using vibrating-sample magnetometer (VSM) at 303 K. The magnetic saturation (Ms) of the two samples at magnetic field of 8.0×10^5 Am^{-1} was 72.2 Am^2 kg^{-1} for $CoFe_2O_4$ and 63.2 Am^2 kg^{-1} for $CoFe_2O_4$–NH_2 (Fig. 5A). The magnetization curves of the amine-functionalized ferrite ($CoFe_2O_4$–NH_2) show a narrow hysteresis loop with low coercivity (Hc: 4.2×10^3 Am^{-1}) and remanent magnetization (Mr) 2.2 Am^2 kg^{-1}. In the case of non-functionalized cobalt ferrite, a wider hysteresis loop can be found on the VSM curve, the coercivity is 1.41×10^4 Am^{-1} next to 12.0 Am^2kg^{-1} Mr value, as can be seen in the insert of Fig. 5A. The values of coercivity (Hc) and the remanence (Mr) were similar to those reported in the literature, where the following ranges are given: Hc = $4 \cdot 10^4$–$1.2 \cdot 10^5$ Am^{-1} (~ 500–1500 Oe), Ms = 13–61 Am^2 kg^{-1} (emu g^{-1}) and Mr: 5–27 Am^2 kg^{-1} (emu g^{-1})[35]. The obtained Hc and Mr values indicate the ferromagnetic nature of the two ferrite samples. Narrow hysteresis loops indicate that the samples can be readily demagnetized and efficiently separated using an external magnetic field, as can be seen in Fig. 5B. The Ms values are lower than the reported value for the bulk cobalt ferrite (80 emu g^{-1})[36]. Owing to the small particle size, the finite-size effect becomes more pronounced, resulting in lower Ms values for the nanoparticles compared to the bulk phase of cobalt ferrite[37]. The saturation magnetization and remanent magnetization

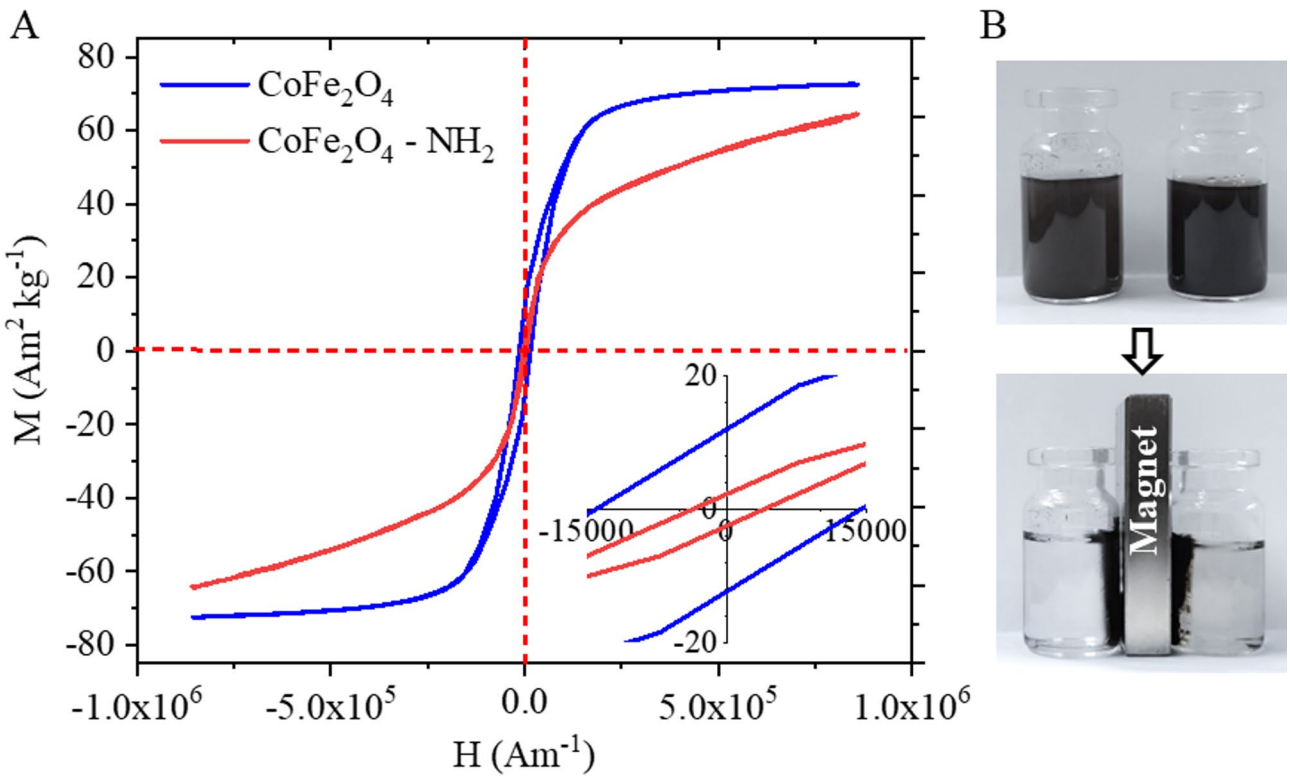

Fig. 5 Magnetization curves of $CoFe_2O_4$–NH_2 the non-functionalized $CoFe_2O_4$ (**A**), and their magnetic separability (**B**).

differ between the two $CoFe_2O_4$ nanoparticle samples produced by different methods, which can be attributed to their significantly different particle sizes. The average size of the nanoparticles 51 ± 8 nm ($CoFe_2O_4$·NH_2) ($CoFe_2O_4$) (Fig. 2).

Adsorption tests of the cobalt ferrite nanoparticles with toxic metal ions

The time- and pH-dependence experiments were carried out with solutions containing lead ions (Fig. 6). The adsorption equilibrium was reached within approximately 60 min; therefore, a contact time of 60 min was considered sufficient for the adsorption process (Fig. 6A). We also monitored the leaching of cobalt and iron from the applied adsorbents. In the time-dependence study, a slight increase was observed with increasing shaking time however, this is still a small amount, only a few mg/L.

Using the time-dependent adsorption data, the kinetic behavior was evaluated with the pseudo-first-order (PFO) and pseudo-second-order (PSO) models, which are among the most widely applied rate equations in adsorption studies. Although the PFO model is frequently used as an initial descriptor of adsorption rates, several authors have noted that it often underestimates the equilibrium uptake and provides weaker correlation coefficients, particularly for systems governed by chemisorption. The PSO model is considered more appropriate for describing metal-ion adsorption on oxide-based nanomaterials[38–40].

Both kinetic models were applied in the present work to assess the adsorption mechanism of the $CoFe_2O_4$ and amine-functionalized $CoFe_2O_4$ samples (SI Fig. 3). For the unmodified cobalt ferrite, the PFO model yielded a rate constant of $k_1 = 1.96 \times 10^{-2}$ min^{-1}, an underestimated equilibrium capacity of $q_e = 16.9$ mg/g, and a moderate correlation ($R^2 = 0.7798$). The amine-functionalized sample showed a slightly improved PFO fit with $k_1 = 1.89 \times 10^{-2}$ min^{-1}, $q_e = 19.6$ mg/g, and $R^2 = 0.8848$. In both cases, the PFO model significantly underestimated the experimentally observed equilibrium capacities.

In contrast, the PSO model provided a better description of the kinetic data for both materials. For cobalt ferrite, the PSO analysis resulted in an equilibrium capacity of $q_e = 62.1$ mg/g, a rate constant of $k_2 = 2.8 \times 10^{-3}$ g mg^{-1} min^{-1}, and a very high correlation coefficient ($R^2 = 0.9977$). The amine-functionalized sample exhibited an even higher equilibrium capacity and a slightly larger rate constant, yielding $q_e = 80.6$ mg/g, $k_2 = 3.1 \times 10^{-3}$ g mg^{-1} min^{-1}, and $R^2 = 0.9986$.

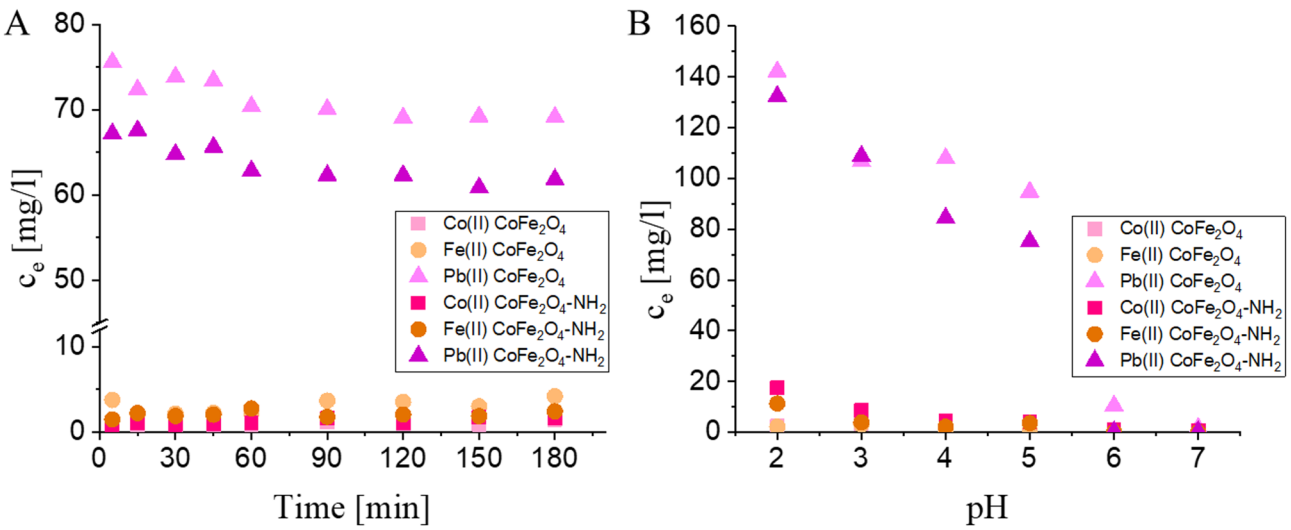

Fig. 6 Time- (**A**) and pH- (**B**) dependent adsorption of lead ions on non-functionalized (light colour) and amine-functionalized (dark colour) $CoFe_2O_4$ magnetic adsorbents.

During the pH-dependence experiment, we found that increasing pH led to a higher amount of adsorbed lead ions. The pH affects both the distribution of adsorbate species and the surface charge of the adsorbent, playing a crucial role in the adsorption process[41]. The pH-dependent adsorption of Pb(II) on both $CoFe_2O_4$ and $CoFe_2O_4$–NH_2 can be explained by the protonation state of the surface groups and the speciation of lead in solution. At low pH, the –OH and –NH_2 groups on the nanoparticle surface are predominantly protonated, resulting in strong competition between H^+ and Pb^{2+} ions and reduced accessibility of coordination sites. Consequently, the adsorption capacity is low under acidic conditions. As the pH increases toward 5, partial deprotonation occurs and oxygen donor groups and lone-pair-bearing amine functionalities become available enabling the formation of inner-sphere complexes with Pb^{2+}. This reduction in proton competition, together with the appearance of deprotonated ligands, leads to a marked increase in adsorption capacity. Similar trends have been reported for cobalt ferrite systems[42,43], where the transition from protonated to deprotonated surfaces is the key factor governing pH-dependent adsorption.

At pH = 5, used in all subsequent experiments, precipitation of $Pb(OH)_2$ is not expected, as it typically occurs only above pH ≈ 6–7. The higher adsorption capacity of the amine-functionalized sample can be attributed to the additional –NH_2 groups, which provide stronger and more numerous coordination sites for Pb(II) compared to the non-functionalized $CoFe_2O_4$.

The metal ion concentration also affects the adsorption capacity[44]. The results of the concentration-dependent experiments show that the adsorbed metal ion amount increased with increasing initial concentration. We obtained different types of results for each ion (Pb(II); Cd(II) and Ni(II)). While the lead ions (Fig. 7A) showed a clearly defined isotherm with a maximum, in the case of nickel ions (Fig. 7C) the results indicated a linear-like relation,

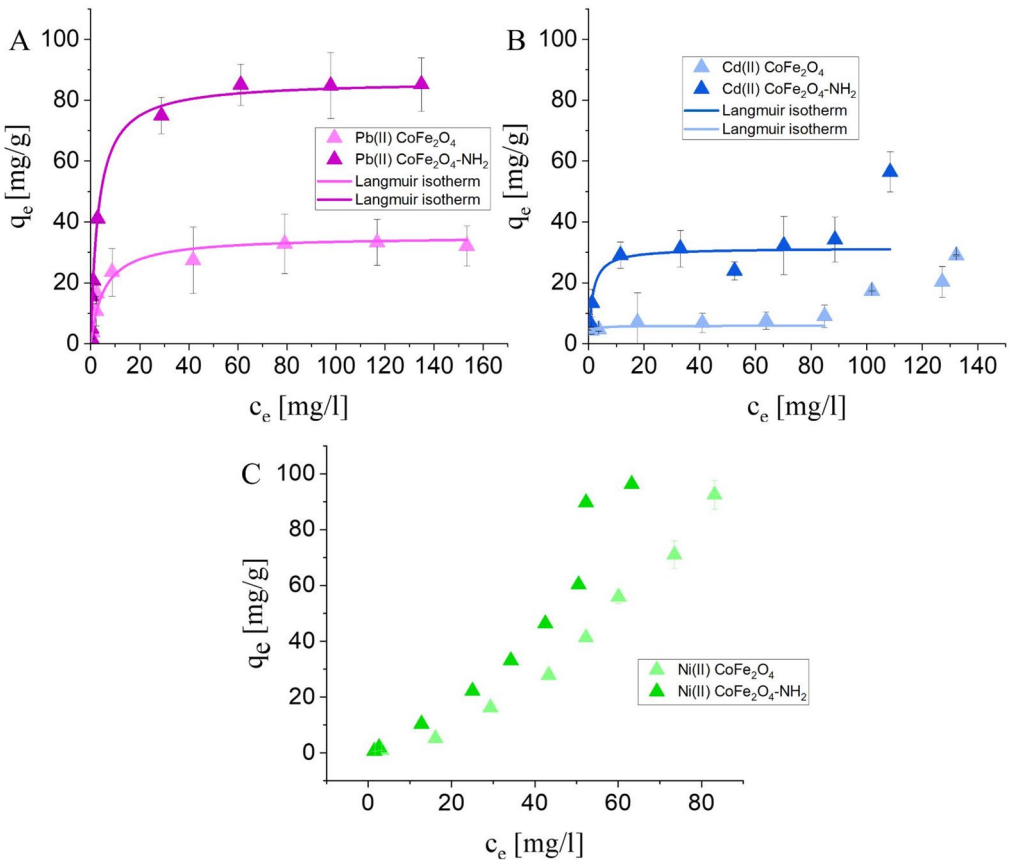

Fig. 7 Adsorption results of Pb^{2+} (**A**), Cd^{2+} (**B**), and Ni^{2+} (**C**) ions on functionalized (dark colour) and non-functionalized (light colour) $CoFe_2O_4$ adsorbents, along with the fitted Langmuir isotherms.

and for cadmium ions (Fig. 7B) they suggested the formation of multilayer adsorption. A possible explanation for the observed differences in adsorption is that the ionic radius and hydration enthalpy of the metal ions play a key role. For Pb^{2+}, Cd^{2+}, and Ni^{2+}, the ionic radius increases while the hydration enthalpy decreases in the order $Ni^{2+} < Cd^{2+} < Pb^{2+}$, meaning smaller ions like Ni^{2+} are more strongly hydrated, whereas larger ions like Pb^{2+} are less hydrated and more easily adsorbed onto surfaces[45].

What also clearly emerged from the experiments is that the amine-functionalized $CoFe_2O_4$ possesses a higher adsorption capacity than their counterpart without functional groups. Several studies have demonstrated that amine functionalization can significantly enhance the adsorption capacity of certain adsorbents. This improvement is attributed to the superior complexation ability of adsorbents bearing these functional groups[46–48].

The Langmuir model has frequently been reported to provide a good fit for metal ion adsorption, particularly in cases where the isotherms exhibit saturated monolayer adsorption, characteristic of a type I isotherm[49]. By fitting the experimental results obtained with lead ions to the Langmuir isotherm, the maximum adsorption capacity was determined to be 34.5 ± 5.3 mg/g for the non-functionalized adsorbent, whereas the functionalized adsorbent exhibited more than twice this value (86.4 ± 1.5 mg/g). In the case of cadmium ions, however, the results indicated multilayer adsorption, and the Langmuir model was therefore not fully applicable. Fitting the data only up to the first plateau yielded adsorption capacities of 31.4 ± 4.2 mg/g and 5.9 ± 0.8 mg/g for the functionalized and non-functionalized adsorbents, respectively. In the case of nickel ions, fitting the Langmuir isotherm could not be achieved.

The isotherm analysis (SI Table 2.) revealed clear ion-dependent behaviour for the three metal ions. For Pb^{2+}, all applied models - Langmuir, Freundlich, Temkin and Redlich–Peterson - provided acceptable fits, with the amine-functionalized sample consistently showing higher affinity and capacity. In contrast, Cd^{2+} exhibited weaker correlations, and only the Freundlich and Temkin models yielded meaningful parameters, indicating a more heterogeneous adsorption process. For Ni^{2+}, the data followed a nearly linear trend, and only the Freundlich model could be fitted reliably, reflecting low affinity and the absence of monolayer saturation.

Based on these results, it is not surprising that in the presence of competing metal ions (Fig. 8.), Pb(II) adsorption remained dominant, while Cd(II) showed partial competition and Ni(II) was barely adsorbed. This behavior reflects the combined effects of ion hydration energy, ionic radius, and the preferential complexation of Pb(II) with surface amine groups, indicating a pronounced selectivity of both $CoFe_2O_4$ and $CoFe_2O_4$–NH_2 toward lead ions under multicomponent conditions. The advantage of amine functionalization was also evident here, with a significant difference observed in the amount of lead ions adsorbed.

A similar trend was reported by Godwin et al. for ZnO/goethite nanocomposites investigated in Cd(II)–Pb(II) and Cd(II)–Pb(II)–Ni(II) ternary systems, where Pb^{2+} showed the highest adsorption capacity, followed by Cd^{2+}, while Ni^{2+} displayed significantly lower uptake. The authors attributed this behavior primarily to differences in hydration energy and ionic radius, with Pb^{2+} being less strongly hydrated and therefore more competitive for surface binding sites[50].

Further evidence for Pb(II) dominated adsorption on magnetic nanoparticles was provided by Yang et al., who studied amino- and carboxyl-functionalized Fe_2O_4 nanoparticles in competitive Pb^{2+}/Cd^{2+} systems. The authors demonstrated a strong preferential adsorption of Pb^{2+} on amino-functionalized surfaces, which they explained

Table 2 Adsorption performance of nanoparticles during first use (lines 1–2) and reuse after heat treatment (line 3). Values represent mean ± standard deviation where applicable.

$CoFe_2O_4$–NH_2 concentration [mg/mL]	Initial cell concentration (before adsorption) [cfu/mL]	Supernatant cell concentration (after adsorption) [cfu/mL]	Adsorption efficiency [%]
First use			
30	**$2.1 \pm 0.7 \times 10^2$**	**No detectable colonies**	**100**
3	**1.6×10^2**	**No detectable colonies**	**100**
Reuse after heat treatment			
30	**$3.6 \pm 1.1 \times 10^2$**	**No detectable colonies**	**100**

Significant values are in bold.

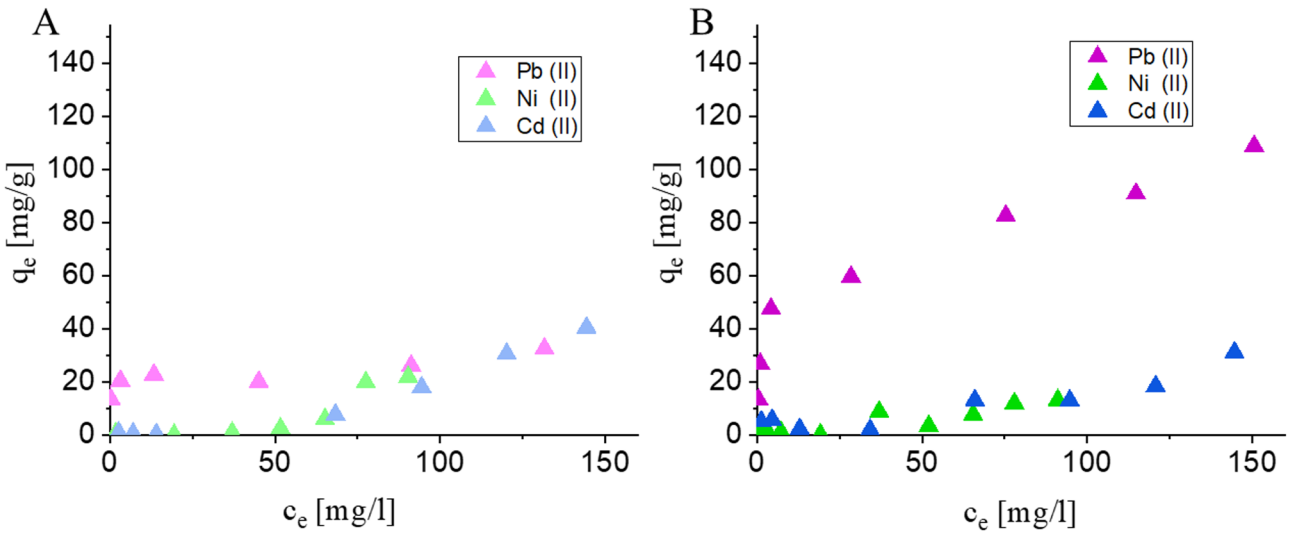

Fig. 8 Multicomponent ion adsorption on $CoFe_2O_4$ adsorbents: non-functionalized (**A**) and amine-functionalized (**B**).

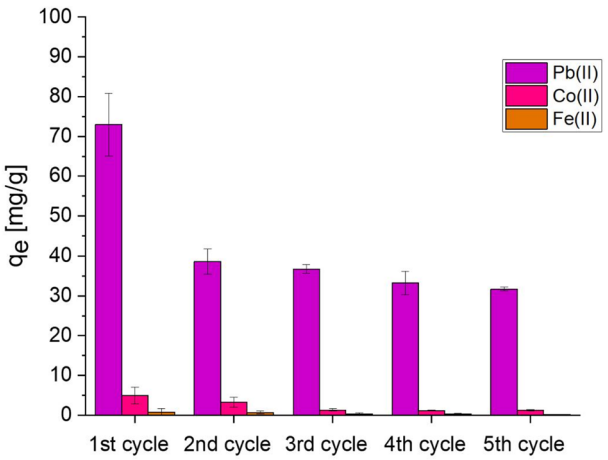

Fig. 9 Reuse adsorption tests with Pb(II) ions on amine-functionalized $CoFe_2O_4$ adsorbents.

by inner-sphere complex formation and HSAB-based coordination between Pb^{2+} and surface $–NH_2$ groups. This mechanism closely aligns with our observation that amino functionalization enhances Pb^{2+} selectivity in multicomponent solutions, indicating that surface complexation plays a key role beyond simple electrostatic attraction[51].

Comparable conclusions were also reported by Kaur et al., who investigated ferrite-based nanocomposites in the presence of multiple competing metal ions, including Pb^{2+}, Cd^{2+}, and Ni^{2+}. Their results showed that Pb^{2+} preferentially occupied high-affinity adsorption sites, while Ni^{2+} had minimal impact on overall adsorption performance[52].

This agreement with our results highlights the general nature of Pb^{2+} preference in ferrite- and metal-oxide-based nanomaterials.

Reuse experiments with Pb(II) solutions on the amine-functionalized adsorbent showed a significant decrease (35 mg/g) in adsorption capacity after the first cycle, decreasing from an initial value of about 73 mg/g (Fig. 9). After this initial decline, the reused adsorbent maintained a relatively constant adsorption capacity of around 30 mg/g over several consecutive cycles. Compared to the amount of adsorbed lead ions, minimal cobalt and even less iron leaching was measured from the adsorbents. Notably, no regeneration protocol was applied between cycles; the material was only dried prior to reuse. These observations suggest that partial saturation may occur

during repeated operation. Future studies will therefore focus on implementing and optimizing regeneration strategies to improve long-term reusability and maintain high adsorption performance. Given the superior adsorption performance of the amine-functionalized cobalt ferrite nanoparticles toward toxic metal ions, subsequent investigations on bacterial adsorption were carried out exclusively using the functionalized material.

Adsorption tests of the amine-functionalized cobalt ferrite nanoparticles with bacterial cells

In the adsorption experiments, the amine-functionalized cobalt ferrite nanoparticles were tested at two different concentrations, 30 mg/mL and 3 mg/mL. These concentrations were selected based on our previous studies, where similar magnetic nanoparticle systems exhibited highly efficient bacterial removal at these dosage levels[53]. The higher concentration (30 mg/mL) was previously shown to ensure complete bacterial removal from aqueous media, while the lower concentration (3 mg/mL) was included to evaluate the adsorption efficiency at a reduced adsorbent dosage.

In the experiments conducted, the initial bacterial cell concentration (before homogenization with the adsorbent) ranged between 1.6×10^2 and 3.6×10^2 cfu/mL. This relatively low initial bacterial concentration was intentionally selected to enable reliable colony counting and quantitative evaluation of the residual non-adsorbed cells in the supernatant after magnetic separation, even in the case of partial adsorption. After incubation of the bacterial suspension with the magnetic nanoparticles, the adsorbent was magnetically separated, and the remaining bacterial cells in the supernatant were quantified by plating on LB agar. The results revealed (Table 2) that no bacterial colonies were detected in the plated supernatant samples, suggesting that the concentration of non-adsorbed cells was below the detection limit of the plating assay. This indicates the absence of detectable *E. coli* cells in the supernatant fraction (Fig. 10). As illustrated in Fig. 10, numerous bacterial colonies were observed on the agar plates before the adsorption experiment, whereas no colonies appeared on plates prepared from the supernatant after adsorption, demonstrating the effective removal of bacterial cells from the aqueous phase. In contrast, viable colonies could still be recovered from the nanoparticle-containing solid fraction after magnetic separation, supporting that the bacterial cells were transferred from the aqueous phase to the adsorbent-associated solid phase during the adsorption process.

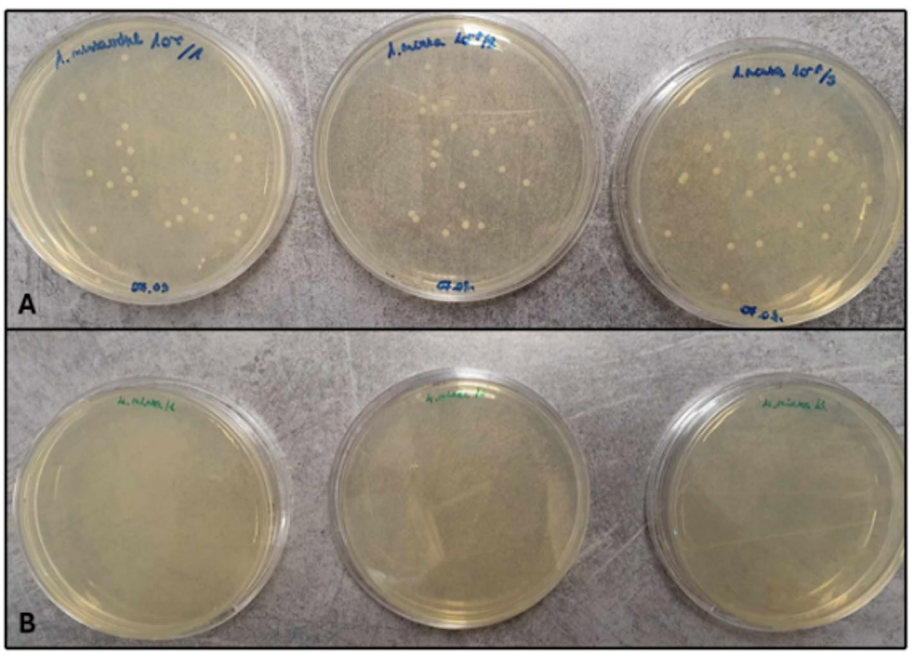

Fig. 10 (**A**) 100 µl of the initial *E. coli* cell suspension (serially diluted to obtain countable colonies; cell concentration: 3.2×10^2 cfu/mL) plated in triplicate on LB agar; (**B**) 100 µl of the supernatant after adsorption from of the dispersions kept on the magnetic holder (no detectable colony-forming units detected).

Importantly, complete removal was achieved not only at 30 mg/mL, but also at the tenfold lower nanoparticle concentration of 3 mg/mL, indicating that high adsorption efficiency was maintained even at substantially reduced adsorbent dosage under the investigated conditions.

These experiments demonstrated that the $CoFe_2O_4$–NH_2 dispersion at concentrations of 30 mg/mL and 3 mg/mL effectively adsorbed *E. coli* cells, thus facilitating the removal of these microorganisms from aqueous media.

The reuse of the $CoFe_2O_4$–NH_2 magnetic nanoparticles was evaluated over five consecutive adsorption cycles. Prior to each reuse step, the recovered particles were thermally treated (120 °C for 2 h) to eliminate previously adsorbed bacterial cells, as described in the Methods section. After each reuse cycle, adsorption was observed to occur with full efficiency, as the initial cell concentration of $3.6 \pm 1.2 \times 10^2$ decreased to zero. This indicates that the cobalt ferrite particles retained their adsorption capacity, confirming the successful reuse of the adsorbent.

The reuse experiments were conducted using the 30 mg/mL nanoparticle concentration. This dosage was selected as a representative model to demonstrate the structural and functional stability of the $CoFe_2O_4$–NH_2 particles over multiple cycles. Since the adsorption mechanism and the chemical integrity of the amine-functionalized surface is expected to remain identical for both tested concentrations (3 and 30 mg/mL), the results obtained at the higher dosage can be reliably extrapolated to the lower one. Furthermore, utilizing the 30 mg/mL concentration ensured easier experimental handling and minimized the impact of potential material loss during the consecutive magnetic separation and recovery steps. These results demonstrate the stability and practical reusability of the amine-functionalized cobalt ferrite nanoparticles for repeated bacterial removal applications.

The highly efficient removal of *E. coli* cells can be primarily attributed to the specific surface chemistry of the amine-functionalized cobalt ferrite nanoparticles. In aqueous media, the amino groups (–NH_2) present on the surface of the $CoFe_2O_4$–NH_2 particles undergo protonation, resulting in a positively charged surface[54]. This positive surface charge enables strong electrostatic interactions with the negatively charged components of the bacterial cell envelope, such as lipopolysaccharides and membrane-associated proteins[55,56]. These interactions promote the rapid attachment of the bacterial cells to the nanoparticle surface, resulting in stable MNP-cell complexes that can be readily removed by magnetic separation[57].

To distinguish this physical adsorption process from chemical inactivation, the integrity and viability of the adsorbed bacteria were evaluated. Following the adsorption experiment, the nanoparticle-bacteria complex (pellet) was resuspended and plated onto LB agar. The subsequent growth of numerous bacterial colonies directly indicates that the cells remained viable while bound to the adsorbent surface. Furthermore, ICP-OES analysis confirmed minimal leaching of cobalt and iron ions during the adsorption process, suggesting that metal-ion-induced toxicity did not play a significant role in the removal efficiency. These results strongly suggest that the observed bacterial removal is predominantly associated with a physical capture mechanism rather than bactericidal action. Such a mechanism is particularly advantageous for water remediation, as it facilitates the removal of intact pathogens without the risk of cell lysis and the subsequent release of intracellular toxins into the treated water[58]. Although cobalt ferrite nanoparticles have frequently been reported to exhibit antibacterial activity through ROS generation, membrane disruption, and metal ion release[59], the present results suggest that these mechanisms were not dominant under the applied experimental conditions. This interpretation is also consistent with our previous observations, where non-silver-containing cobalt ferrite nanoparticles did not exhibit detectable antibacterial inhibition zones, suggesting limited intrinsic antibacterial activity in the absence of additional biocidal components[53]. Additional ROS-specific analyses would be required in future studies to fully exclude oxidative stress-related contributions.

Nevertheless, it should be noted that the present experiments were conducted using relatively low initial bacterial concentrations and a single bacterial model strain under simplified laboratory conditions. Therefore, the maximum bacterial loading capacity and broader applicability of the adsorbent require further investigation.

Adsorption mechanisms

Toxic metal adsorption involves several physical and chemical processes, such as ion exchange, complexation, electrostatic attraction, and surface precipitation. The adsorption kinetics, which depend on factors like contact time, temperature, and concentration, play a key role in determining how fast and effectively metals are removed[60].

The kinetic, pH-dependent and surface charge measurements collectively provide clear evidence for a chemisorption-controlled adsorption mechanism on both $CoFe_2O_4$ and $CoFe_2O_4$–NH_2.

The pseudo-second-order (PSO) model yielded excellent correlation coefficients and realistic equilibrium capacities for both materials. Although the PSO fit is frequently cited in the literature to suggest that the rate-limiting step might be governed by valence-controlled interactions involving electron sharing or exchange between the adsorbent surface and the metal ions[39,40,61], several reviews have clearly demonstrated that such mechanistic interpretations cannot be derived from empirical kinetic models. Lima et al.[62] and Kumar[63] explicitly emphasize that pseudo-second-order kinetics do not imply chemisorption, valence interactions, or inner-sphere complexation, and that kinetic equations must not be used to assign adsorption mechanisms. Therefore, in accordance with these recommendations, the PSO model in the present study is interpreted as an empirical descriptor of the adsorption rate, without mechanistic implications.

The pH of the medium significantly influences both the distribution of adsorbate species and the surface charge of the adsorbent, playing a key role in the adsorption process[64]. The pH-dependent adsorption of Pb(II) on both $CoFe_2O_4$ and $CoFe_2O_4$–NH_2 surfaces can be explained by the protonation state of the surface groups and the speciation of lead in the solution. At low pH, the –OH and –NH_2 groups on the nanoparticle surfaces are predominantly protonated, resulting in strong competition between H^+ and Pb^{2+} ions and causing electrostatic repulsion[65,66]. Consequently, the adsorption capacity is low under highly acidic conditions. As the pH increases towards 5, partial deprotonation occurs, enabling coordination through oxygen donor groups and amine lone pairs, which facilitates the formation of stable inner-sphere coordination complexes with Pb^{2+}[51,67]. The reduction in proton competition, coupled with the emergence of these deprotonated ligands, leads to a significant increase in adsorption capacity, reaching 86.4 mg/g for the functionalized ferrite. The absence of hydroxide precipitation at pH = 5 confirms that removal proceeds through surface binding rather than precipitation[43].

Zeta potential measurements revealed a pronounced shift from negative to positive values after Pb^{2+} adsorption, demonstrating effective charge compensation and the formation of inner sphere complexes at the solid–liquid interface[68]. Amine functionalization further enhances this process by increasing both the density and accessibility of coordination sites, as evidenced by the higher specific surface area, pore volume and nitrogen content of $CoFe_2O_4$–NH_2, which together account for its more than twofold increase in Langmuir capacity for Pb^{2+}[69].

The observed selectivity sequence $Pb^{2+} \gg Cd^{2+} > Ni^{2+}$ is consistent with differences in ionic radius and hydration enthalpy, whereby the larger and less strongly hydrated Pb^{2+} ion more readily undergoes partial dehydration and forms stable inner-sphere complexes with surface O/N donor groups, while the strongly hydrated Ni^{2+} ion interacts mainly through weaker, non-specific adsorption[70]. Taken together, these findings demonstrate that the adsorption of Pb^{2+} on both materials is dominated by inner-sphere surface complexation on deprotonated hydroxyl and amine groups, with chemisorption as the governing mechanism.

In contrast, the removal of bacterial cells is primarily governed by a physical capture mechanism. In the aqueous medium, a sufficient portion of the amine groups remains protonated[54], creating locally positively charged surface regions. This leads to strong electrostatic attraction with the negatively charged components of the *E. coli* cell wall[71]. To summarize these distinct pathways a schematic illustration (Fig. 11.) is presented, highlighting the dual role of amine functionalization acting as a chemical ligand for metal complexation and enabling electrostatic attraction for microorganisms.

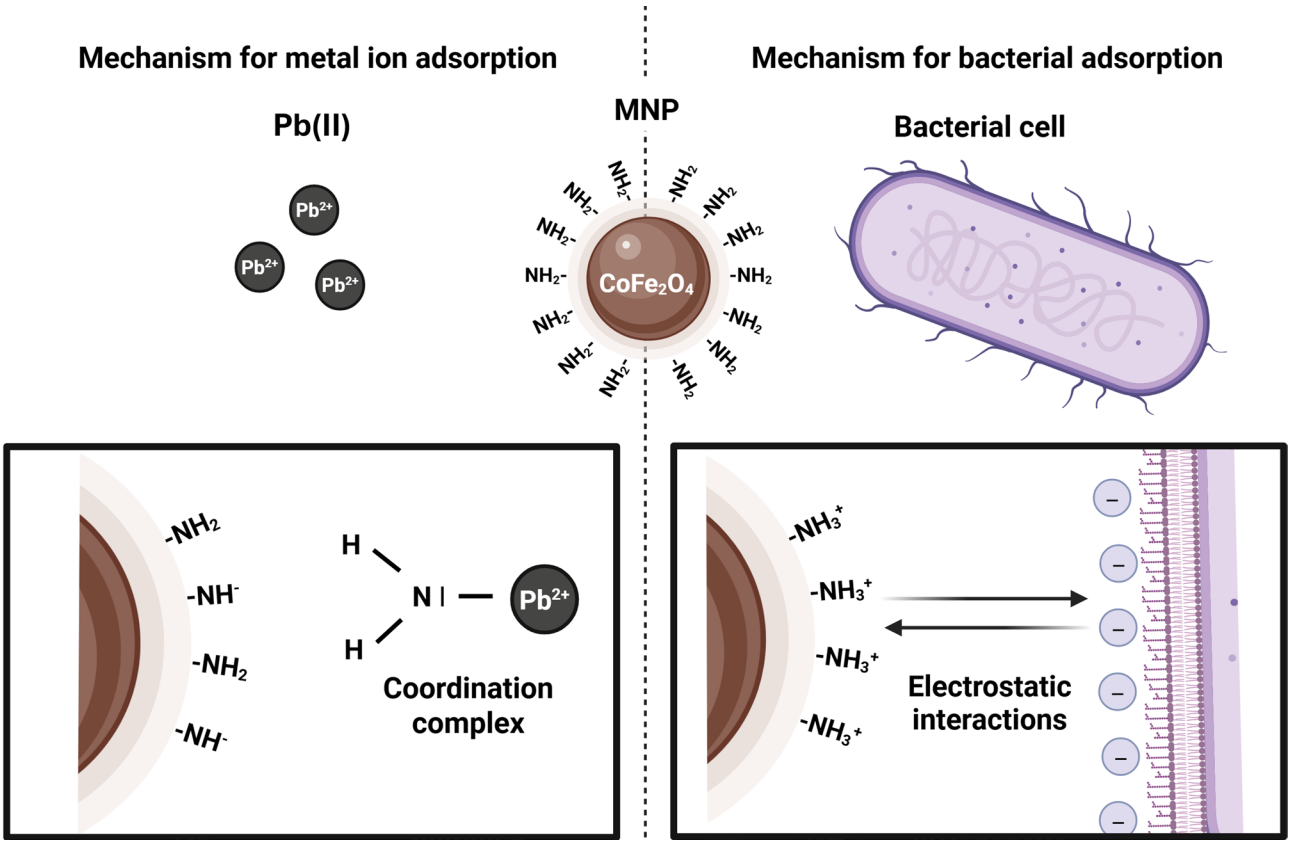

Fig. 11 Schematic illustration of the adsorption mechanisms of metal ions and bacteria on $CoFe_2O_4$–NH_2 MNP (magnetic nanoparticles).

Comparison with literature and relevance to complex water matrices

The obtained results were further evaluated in the context of previously reported ferrite-based adsorption systems. Table 3 shows that the Pb(II) uptake of $CoFe_2O_4$–NH_2 lies at the upper end of the values typically observed for cobalt ferrites, which is consistent with its markedly higher surface area and pore volume.

This contrasts with the dense, low-porosity nanoparticles typically obtained through conventional solvothermal syntheses, such as those described in[72] where excellent crystallinity is achieved but textural properties remain limited. A comparison with the amine-modified ferrite system of Saleem et al.[43] further highlights the distinct behaviour of our material. While their composite shows high capacities for several metal ions, the adsorption is less ion-selective. In contrast, $CoFe_2O_4$–NH_2 exhibits strongly ion-dependent uptake, with high affinity toward Pb(II), multilayer adsorption for Cd(II), and nearly linear behaviour for Ni(II). This ion-specific response reflects the combined influence of surface amine groups, hierarchical micro–mesoporosity, and the differing hydration and complexation tendencies of the metal ions.

Comparison of our bacterial adsorption findings with available literature (Table 4) indicates that the $CoFe_2O_4$–NH_2 particles synthesized in this work exhibit highly efficient E. coli adsorption under the investigated conditions. While previous studies reported lower adsorption efficiencies (e.g., 65% at 2 mg/mL[30], the present material achieved complete (100%) removal at both 3 and 30 mg/mL dosages. This high efficiency is consistent with the results of other amine-functionalized synthesized systems (Fe_3O_4–NH_2), which have also demonstrated strong bacterial binding under comparable conditions. Furthermore, the fact that the adsorbent maintained full adsorption efficiency over five consecutive reuse cycles indicates that the electrostatic binding sites on the amine-functionalized surface remain functionally active after the recovery process.

Table 3 Comparison of the toxic metal adsorption capacity of different ferrite nanoparticles.

Adsorbent	Adsorptive	Max adsorption capacity mg/g	Max adsorption capacity mmol/g	References
$MgFe_2O_4$ amine functionalized	Cu(II)	55.73	0.877	[8]
	Pb(II)	148.15	0.715	
	Zn(II)	50.23	0.768	
$ZnFe_2O_4$ reduced graphene oxide	Pb(II)	89.9	0.4338	[18]
$NiFe_2O_4$ reduced graphene oxide	Pb(II)	121.95	0.3774	[45]
	Cr(III)	126.58	0.7994	
Fe_3O_4–NH_2-COOH	Pb(II)	125.3	0,6047	[51]
	Cd(II)	98.7	0,8780	
$CoFe_2O_4$	Pb(II)	63.1	0.3045	[9]
$MgFe_2O_4$	Co(II)	135.54	2.30	[6]
	Mn(II)	85.69	1.56	
	Ni(II)	52.23	0.89	
	Cu(II)	29.23	0.46	
$Co_{0.6}$ $Fe_{2.4}O_4$	Pb(II)	80.32	0,3876	[43]
$CoFe_2O_4$	Pb(II)	34.5	0.167	This work
	Cd(II)	5.9	0.053	
$CoFe_2O_4$–NH_2	Pb(II)	86.4	0.417	This work
	Cd(II)	31.4	0.279	

Table 4 Comparison of the bacterial adsorption efficiency of different ferrite nanoparticles.

Adsorbent	Adsorptive	Initial cell concentration [cfu/mL]	Adsorption efficiency [%]	Reference
$CoFe_2O_4$–NH_2 [2 mg/mL]	*E. coli*	1×10^7	65	[30]
	S. aureus	1×10^7	95	
$CoFe_2O_4$–NH_2 [0.5 mg/mL]	*E. coli*	1×10^4	93	[53]
$CoFe_2O_4$–NH_2 [1 mg/mL]	*E. coli*	1×10^4	97	
Fe_3O_4–NH_2 [0.15 mg/mL]	*E. coli*	1×10^3	100	[81]
	E. faecalis	1×10^3	100	
PEI modified Fe_3O_4·SiO_2 [40 µg/mL]	*E. coli*	1×10^1	90	[82]
Chitosan coated Fe_3O_4 [0.5 mg/mL]	*E. coli*	1×10^5	98	[31]
	S. enteritidis	1×10^5	32	
$CoFe_2O_4$–NH_2 [30 mg/mL]	*E. coli*	2.1×10^2	100	This work
$CoFe_2O_4$–NH_2 [3 mg/mL]	*E. coli*	1.6×10^2	100	This work

Overall, the $CoFe_2O_4$–NH_2 adsorbent performs competitively with previously reported cobalt ferrite systems, demonstrating the benefits of the present synthesis strategy and its suitability as a multifunctional platform for water remediation.

The behaviour of magnetic nanomaterial-based adsorbents in real wastewater matrices is strongly influenced by the presence of competing ions, dissolved organic matter, and co-existing pollutants. Studies conducted on structurally and functionally related magnetic adsorbents provide clear evidence that matrix complexity can alter adsorption capacity, selectivity, and surface reactivity. Yahya et al. demonstrated that cobalt–ferrite supported activated carbon maintained high removal efficiencies for Pb(II) and Cr(II) in tannery wastewater; however, the relatively modest Langmuir capacities (6.27 and 23.6 mg/g) suggest that background ions partially occupied active sites or interfered with metal–surface complexation, highlighting the competitive nature of multicomponent effluents[73].

Syed et al. reported exceptionally high adsorption capacities for Pb, Hg, and Cd using graphene oxide–coated silver nanoparticles in refinery wastewater, yet their findings also indicated that hydrocarbons and surfactants influenced nanoparticle dispersion and surface accessibility. These observations underline that organic contaminants can modify the physicochemical environment of the adsorbent, affecting both the kinetics and thermodynamics of metal uptake[74].

Oladimeji et al. showed that magnetic graphene oxide retained 90.2% Pb(II) removal efficiency in foundry wastewater despite the presence of oils, suspended solids, and competing ions. Their results confirm that adsorbents with robust surface chemistry and strong metal-binding affinity can maintain high performance even under severe matrix interference, while magnetic separability ensures operational practicality in turbid or particulate-rich waters[75].

Almomani demonstrated that hyperbranched polyglycidol-functionalized magnetic nanoparticles effectively removed Ni(II), Al(III), and Cu(II) from secondary effluent, although the presence of natural organic matter and co-existing ions influenced adsorption behaviour. The removal percentage of the studied toxic metals were slightly affected (maximum decrease: 6.5%) by increasing in the organic matter (from COD = 0 to 110 mg/L) concentration, which can be considered as acceptable reduction considering the water quality parameters. The study highlighted two dominant inhibitory mechanisms: (i) competitive complexation of metal ions by dissolved organic ligands, reducing their free ionic concentration, and (ii) surface fouling, which blocks active sites or alters surface charge. These effects are particularly relevant for adsorbents whose performance relies on electrostatic attraction or outer-sphere complexation[76].

Abdelmegeed et al. reported that amine-functionalized $Fe_3O_4/SiO_2–NH_2$ maintained a high Cu(II) adsorption capacity (229 mg/g) in real industrial wastewater, demonstrating that strong chelating groups such as $–NH_2$ can effectively outcompete background ions and preserve selectivity. Their findings indicate that adsorbents dominated by inner-sphere complexation mechanisms are less susceptible to matrix interference and retain structural and magnetic stability during operation[77].

Taken together, these studies show that competing cations (e.g., Ca^{2+}, Mg^{2+}), anions (e.g., Cl^-, SO_4^{2-}), and natural organic matter can reduce adsorption efficiency through site competition, aqueous complexation, and surface fouling. However, adsorbents functionalized with strong donor groups—such as the amine-modified $CoFe_2O_4–NH_2$ nanoparticles investigated in the present work—are expected to inner-sphere even in complex matrices. Nevertheless, systematic experimental validation in real wastewater matrices containing dissolved organic matter and complex ionic backgrounds will be necessary to fully evaluate the practical applicability of the material.

Materials and methods

Materials

The cobalt ferrite ($CoFe_2O_4$) was synthesized from the following precursors: cobalt(II) nitrate hexahydrate, $Co(NO_3)_2·6H_2O$, MW: 291.03 g/mol (Sigma-Aldrich 63103, Saint Louis, MO, USA); iron(III) nitrate nonahydrate, $Fe(NO_3)_3·9H_2O$ (VWR International, Leuven, Belgium); ethylene glycol, $HOCH_2CH_2OH$, (VWR Int. Ltd., F-94126 Fontenay-sous-Bois, France); monoethanolamine, $NH_2CH_2CH_2OH$ (Merck KGaA, D-64271 Darmstadt, Germany); and sodium acetate, CH_3COONa (ThermoFisher GmbH, D-76870 Kandel, Germany), Poly(ethylene glycol); PEG 400 (VWR Int. Ltd., F-94126 Fontenay-sous-Bois, France). The stock solutions for the adsorption tests were prepared with the following chemicals: lead(II) nitrate, $Pb(NO_3)_2$, MW: 331,21 g/mol (VWR Int. Ltd., 3001 Leuven, Belgium); nickel(II) nitrate hexahydrate $N_2NiO_6 · 6H_2O$, MW: 290,81 g/mol (VWR Int. Ltd., 3001 Leuven, Belgium); cadmium nitrate tetrahydrate, 99+% $CdN_2O_6·4H_2O$, MW: 308.46 g/mol (Thermo Scientific, Massachusetts 02451, USA). The standard solutions used for the ICP measurements were: Lead standard solution (1000 mg/l Pb, lead nitrate in nitric acid 0.5 mol/l, Merck KGaA, 64293 Darmstadt, Germany); Nickel standard solution (1000 g/l Ni, Merck KGaA, 64293 Darmstadt, Germany); Cadmium

standard solution (1000 mg/l Cd, cadmium nitrate in nitric acid 0,5 mol/l, Merck KGaA, 64293 Darmstadt, Germany), Cobalt standard solution (1000 mg/l Co, cobalt nitrate in nitric acid 0,5 mol/l, Merck KGaA, 64293 Darmstadt, Germany), Iron(II) standard solution (1000 g/l Fe, Fluka Chemie GmbH, 9471 Buchs, Switzerland). For bacterial adsorption experiments LB medium, physiological saline, and agar plates were prepared using tryptone and yeast extract (Neogen Culture Media, Lansing, MI, USA), sodium chloride, and bacteriological agar (VWR International, Leuven, Belgium).

Synthesis of non-functionalized and amine-functionalized cobalt ferrite nanoparticles

To prepare amine- and non-functionalized cobalt ferrite magnetic adsorbents two different methods, namely solvothermal and sonochemical synthesis were applied (Fig. 12).

Amine-functionalized cobalt ferrite ($CoFe_2O_4$–NH_2) was synthesized by using a polyol-based, solvothermal synthesis method, at atmospheric pressure at 200 °C. In ethylene glycol (2.7 mol), iron(III) nitrate nonahydrate (20 mmol), cobalt(II) nitrate hexahydrate (10 mmol) and sodium acetate (150 mmol) were dissolved. The solution was heated to 100 °C in a round bottom flask under reflux with continuous stirring; after 30 min, monoethanolamine (MEA, 0.58 mol) was added to this. After 12 h continuous agitation and reflux, the cooled solution was separated by magnetic field, and the solid phase was washed with distilled water several times. Finally, the amine-functionalized cobalt-ferrite samples were rinsed with anhydrous ethanol and were dried at 80 °C overnight.

For the synthesis of the non-functionalized cobalt ferrite ($CoFe_2O_4$) nanoparticles, a two-step process was used, which includes sonochemical treatment and combustion step. In the first step, iron(III) nitrate nonahydrate (14 mmol) and cobalt(II) nitrate hexahydrate (7 mmol) were dissolved in 20 g polyethylene glycol (PEG 400). The solution of the precursors was treated by using a Hielscher UIP1000 Hdt tip homogenizer for 3 min (130 W, 19 kHz). After the sonochemical treatment, from the nitrate precursors formed cobalt(II) hydroxide and iron(III) hydroxide nanoparticles. The second step in the complex synthesis is the combustion process, during which the polyol was burned in a furnace at a temperature of 400 °C. During the treatment, the metal precursors (Co(II) hydroxide and Fe(III) hydroxide) were dehydrated, and a spinel structure ($CoFe_2O_4$) was formed.

Characterization techniques

HRTEM (High-resolution transmission electron microscope) was applied for characterization of particle size and morphology of the cobalt ferrite nanoparticles. Talos F200X G2 electron microscope (Thermo Fisher Scientific Ltd.), with field emission electron gun (X-FEG, accelerating voltage: 20–200 kV) was used. For the imaging and electron diffraction measuring, a SmartCam digital search camera (Ceta 16 Mpixel, 4k × 4k CMOS camera) and

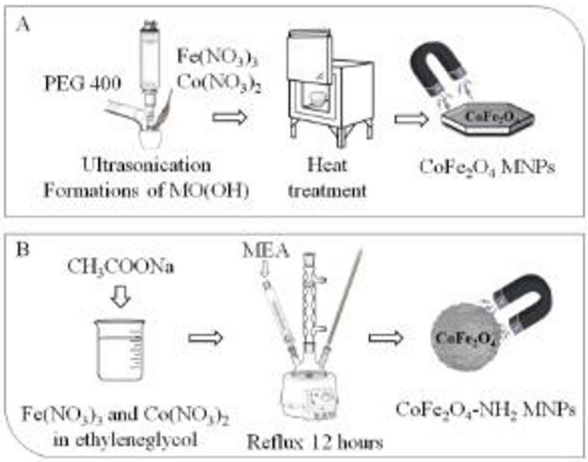

Fig. 12 Synthesis route of non-functionalized (**A**) and amine-functionalized (**B**) cobalt ferrite nanoparticles.

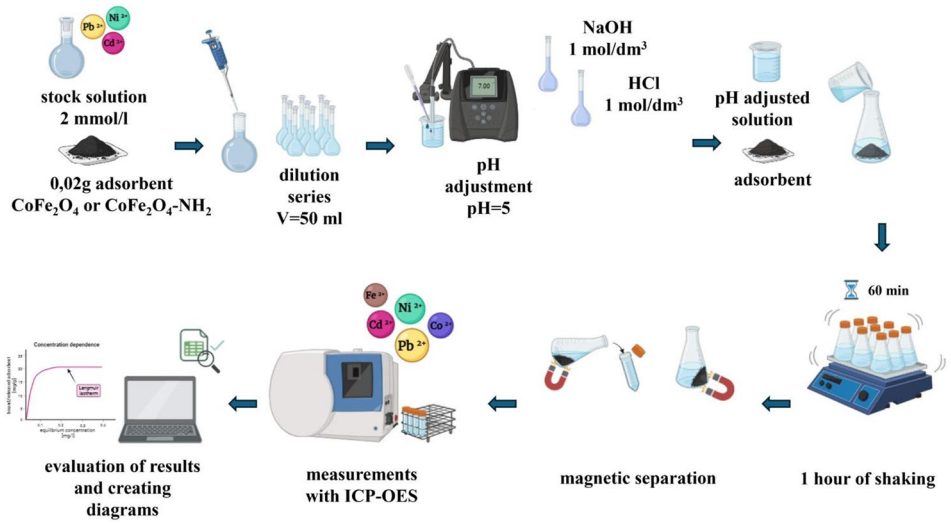

Fig. 13 Process of performing toxic metal ion adsorption tests.

high-angle annular dark-field (HAADF) detector were used. Copper grids (300 mesh) from the Ted Pella Inc. (4595 Redding, CA 96003, USA) were used as sample holders for electron microscopic examination. During the sample preparation, the aqueous dispersion of ferrite was dropped on to the copper grids. To identify and quantification of the crystalline phases of the ferrite samples X-ray diffraction measurements (Bruker D8 diffractometer with Cu-Kα source and Vantec detector). Identification of the surface functional groups of the ferrite nanoparticles was carried out with Fourier transformed infrared spectroscopy (FTIR) by using the Bruker Vertex 70 equipment. During sample preparation, a 10 mg sample was pelletized with 250 mg spectroscopic-grade KBr; the measurements were carried in transmission modeSzöveg beírásához kattintson vagy koppintson ide. Nitrogen adsorption isotherms were measured using an Anton Paar Autosorb 6200 EPDM MP instrument with high-purity nitrogen gas (5.0) at 77 K employing liquid nitrogen. Carbon, hydrogen, and nitrogen contents were measured using an Elementar Vario MACRO CHNS analyzer. Approximately 100 mg of sample was used for each determination, and three parallel measurements were carried out. The electrokinetic (zeta) potential was determined from the electrophoretic mobility via laser Doppler electrophoresis using an Anton Paar Litesizer 500 instrument (Anton Paar GmbH, Graz, Austria). The measurements were performed at 25 °C in automatic mode (for backscatter detector, fixed at 175°; for side scatter, 90° detector angle; for front scatter, 15° detector angle) using a 633 nm He-Ne laser. Samples were measured in polystyrene disposable cuvettes (Anton Paar, Hamburg, Germany). The magnetic characterization of ferrite nanoparticles was carried out using a self-developed (University of Debrecen) vibrating-sample magnetometer (VSM) system based on a water-cooled Weiss-type electromagnet. The powder samples were pelletized for measurements, with a typical mass of 20 mg. The magnetization (M) was measured as a function of the magnetic field (H) up to a field strength of 10,000 Oe at room temperature.

Toxic metal ion adsorption tests of the cobalt ferrite nanoparticles

Adsorption experiments were performed with non-functionalized and amine-functionalized cobalt ferrite nanoparticles. We investigated the adsorption of toxic metals ions like Pb(II), Ni(II) and Cd(II). In addition to monoelement experiments, we also performed multielement tests, where all the toxic metal ions were placed in the same solution. As we know, adsorption is influenced by many parameters. Among these, we examined time, pH and concentration dependence.

First of all, stock solution 2 mmol/l of Pb(II), Ni(II) and Cd(II) were made with distilled water (Fig. 13). Analytical grade $Pb(NO_3)_2$, $Ni(NO_3)_2 \cdot 6H_2O$ and $Cd(NO_3)_2 \cdot 4H_2O$ were used to prepare stock solutions. To investigate the time dependence, 50 ml 0,5 mmol/l solution was measured into Erlenmeyer flasks then 0.02 g adsorbent

was added to the mixture. The prepared solutions were placed on a shaker and removed at predetermined intervals (after 5–180 min) for sampling.

During the pH dependence tests, 0,5 mmol/l solution was used. The pH of the solutions was adjusted between pH2 and pH7 using 1 M HCl and NaOH solutions. 0.02 g of adsorbent was added to the prepared mixtures and the samples were shaken for 1 h.

As a conclusion to the monoelement experiment series we also performed concentration dependence tests. The previously determined 1 h shaking time and pH = 5 were used with the amount of 0.02 g adsorbents. The experiments were carried out between 0.004 and 0.800 mmol/l concentration range.

Since the adsorbent we used have excellent magnetic properties, we separated them from the solution using a magnet in every case. The amount of adsorbed and desorbed metal ions was determined with the help of an Inductively Coupled Plasma Optical Emission Spectroscopy (ICP-OES) machine. After the measurements were completed, Langmuir isotherm was used to determine the maximum adsorption capacity.

The conditions for the multielement adsorption tests were the same as those for the monoelement concentration dependence studies. Here, the stock solution contained all three elements (Pb(II); Ni(II) and Cd(II)) at a concentration of 2 mmol/l.

The reuse experiments were conducted following the same procedure, using solutions with an initial Pb(II) concentration of 0.15 mmol/l. No regeneration step was applied between consecutive cycles; the adsorbent was only dried prior to reuse.

The adsorption kinetics were evaluated using the linearized forms of the pseudo-first-order (PFO) and pseudo-second-order (PSO) models. Experimental q_t values obtained at different contact times were used for both fittings.

For Pseudo-first-order (PFO) model the linearized Lagergren equation was applied:

$$\log(q_e - q_t) = \log q_e - \frac{k_1}{2.303}\, t$$

For each dataset, the term $\log(q_e - q_t)$ was calculated at every time point, and the values were plotted as a function of t. The equilibrium adsorption capacity q_e and the rate constant k_1 were obtained from the intercept and slope of the linear regression, respectively. Only the linear region of the curve was used for fitting to ensure model validity.

For Pseudo-second-order (PSO) model, the Ho–McKay linear form was used:

$$\frac{t}{q_t} = \frac{1}{k_2 q_e^2} + \frac{t}{q_e}$$

For each time point, the ratio t/q_t was calculated and plotted against t. The slope and intercept of the linear regression provided the values of $1/q_e$ and $1/(k_2 q_e^2)$, from which the equilibrium capacity q_e and the rate constant k_2 were determined.

- q_t is the amount of adsorbate taken up at time t (mg g^{-1}).
- q_e is the equilibrium adsorption capacity (mg g^{-1}).
- t- is the contact time (min).
- k_1 is the pseudo-first-order rate constant (min^{-1}).
- k_2 is the pseudo-second-order rate constant (g mg^{-1} min^{-1}).

Adsorption processes are commonly characterized using adsorption isotherms. An adsorption isotherm describes the amount of adsorbate retained on the adsorbent surface as a function of the equilibrium concentration of the solute. The equilibrium concentration is defined as the difference between the total amount of solute introduced into the system and the amount adsorbed. Among the most frequently applied models, the Langmuir isotherm is widely used, which can be expressed by the following equations[79,80]

$$q_e = \frac{q_m \cdot K_L \cdot Ce}{1 + C_e \cdot K_L}$$

where q_e is the equilibrium adsorption capacity (mmol g^{-1} or mg g^{-1}), q_m is the maximum adsorption capacity (mmol g^{-1} or mg g^{-1}), K_L is the Langmuir equilibrium constant, C_e is the equilibrium concentration (mmol L^{-1} or mg L^{-1}).

The Freundlich isotherm is an empirical model commonly applied to heterogeneous surfaces, describing multilayer adsorption according to the following equation:

$$q_e = K_F C_e^{1/n}$$

where q_e is the equilibrium adsorption capacity (mmol g^{-1} or mg g^{-1}),K_F is the Freundlich adsorption constant,$1/n$ is the heterogeneity factor indicating surface non-uniformity,C_e is the equilibrium concentration (mmol L^{-1} or mg L^{-1}).

The Temkin isotherm assumes that the heat of adsorption decreases linearly with surface coverage, and can be expressed as:

$$q_e = B\ln(K_T C_e)$$

whereq_e is the equilibrium adsorption capacity (mmol g^{-1} or mg g^{-1}),B is the Temkin constant related to adsorption energy, K_T is the Temkin equilibrium binding constant,C_e is the equilibrium concentration (mmol L^{-1} or mg L^{-1}),

The Redlich–Peterson isotherm is a hybrid model incorporating features of both Langmuir and Freundlich equations, and is written as:

$$q_e = \frac{K_R C_e}{1 + a_R C_e^{\beta}}$$

where $q_e$is the equilibrium adsorption capacity (mmol g^{-1} or mg g^{-1}), K_R is the Redlich–Peterson constant related to adsorption capacity,a_R is the Redlich–Peterson constant related to adsorption intensity, β is the heterogeneity parameter,C_e is the equilibrium concentration (mmol L^{-1} or mg L^{-1}).

The obtained results were fitted to the listed isotherm using the above-mentioned equation, with the ORIGIN 2018 Graphing & Analysis software (SR1 b9.5.1.195, https://www.originlab.com/2018).

Bacterial adsorption tests of the cobalt ferrite nanoparticles

The LB (Luria–Bertani) medium used for the growth of *E. coli* bacteria was prepared by dissolving the solid constituents (10 g tryptone, 5 g yeast extract, and 10 g sodium chloride) in 1000 mL of ultrapure water under continuous stirring with a magnetic stirrer. The resulting medium was aliquoted into 100 mL Erlenmeyer flasks at a volume of 35 mL per flask, sealed with cotton plugs, and sterilized by autoclaving at 121 °C for 15 min (103–117 kPa). This liquid broth served as the culture medium for preparing the initial bacterial suspensions.

For the preparation of LB agar plates, 15 g of bacteriological agar was added to 1000 mL of LB broth, followed by sterilization in glass bottles. After autoclaving, the molten agar medium was cooled to approximately 50 °C in a water bath and subsequently poured into sterile 90 mm Petri dishes, where it was allowed to solidify. The solidified plates were stored at 4 °C and used within one month. These agar plates were employed as a solid medium for determining the colony-forming units (cfu) to assess both the initial cell concentration and the residual concentration following the adsorption experiments.

Physiological saline solution was employed for dispersing bacterial cells and magnetic nanoparticles. To prepare the saline solution, 8.5 g of sodium chloride was dissolved in 1000 mL of ultrapure water, and the solution was sterilized by autoclaving in glass bottles at 121 °C for 15 min.

For the adsorption experiments *Escherichia coli* ATCC 25922 (Gram-negative) was used. A single, well-isolated bacterial colony was aseptically inoculated into 35 mL of LB medium using a sterile inoculation loop. The culture was incubated in a shaking incubator at 37 °C and 160 rpm for 24 h under optimal growth conditions.

Bacterial cell density was determined by measuring the optical density at 600 nm (OD_{600}) with a NanoDrop™ spectrophotometer (Thermo Fisher Scientific, Waltham, MA, USA), using LB medium as the blank. Since higher OD_{600} values correspond to increased bacterial cell concentrations, these measurements were used to estimate the initial cell density prior to the experiments. To standardize the starting bacterial concentration in all adsorption assays, the cultures were diluted to an OD_{600} value of 0.1.

To determine the cell concentration corresponding to $OD_{600} = 0.1$, a tenfold serial dilution was prepared, and 3×100 µL of the 10^{-6} dilution was spread on LB agar plates. The inoculated plates were incubated at 37 °C in the dark for at least 16 h (overnight) to allow colony formation. Colony counts in the 30–300 colony forming unit (cfu) per plate range were used to calculate the cell concentrations.

The cell concentration determined for the 10^{-6} dilution was used as the initial cell concentration in the experiments, representing the amount of bacterial cells intended to be adsorbed by the adsorbent. This bacterial suspension served as the bacteria-only control, representing the initial cell concentration prior to contact with the magnetic nanoparticles.

Magnetic nanoparticles were tested at two concentrations for *E. coli* adsorption: 30 mg/mL and 3 mg/mL, using 275 µL of the initial $CoFe_2O_4$–NH_2 dispersion (109 mg/mL) for 30 mg/mL, and 27.5 µL $CoFe_2O_4$–NH_2 for 3 mg/mL. These doses were selected based on our previous study involving core-shell structured silver-ferrite nanoparticles[53]. In that work, these concentrations were identified as highly effective benchmarks: 30 mg/mL consistently ensured the complete (100%) removal and inactivation of both Gram-negative and Gram-positive bacteria in aqueous media, while 3 mg/mL was determined as the minimum concentration required to maintain a clear inhibition zone on solid surfaces. By employing these same concentrations, we aimed to maintain methodological consistency and directly compare the adsorption performance of the current amine-functionalized ferrites with the previously reported core-shell systems.

Since the initial MNP dispersion was prepared in water, the solvent was removed via magnetic separation. Following the removal of the aqueous phase, the nanoparticles were resuspended in 900 µL of sterile physiological saline solution to preserve osmotic conditions during cell-based experiments. Subsequently, 100 µL of a 10^{-5} diluted bacterial suspension was added, yielding a final bacterial dilution of 10^{-6} within the ferrite dispersion. After thorough mixing, the samples were rotated for 30 min to promote uniform bacterial adsorption onto the magnetic nanoparticles. The adsorbents were then separated using a magnetic stand for 30 min to allow complete magnetic separation, and three aliquots of 100 µL from the supernatant (containing non-adsorbed bacterial cells) were plated to quantify the concentration of unbound bacteria. The bacterial adsorption efficiency was calculated according to the following equation: adsorption efficiency (%) = (initial cfu − supernatant cfu) / initial cfu × 100.

In separate control experiments performed previously under identical handling conditions, aliquots containing only the magnetic nanoparticle dispersion were plated on LB agar to verify sterility. No bacterial colonies were detected in these controls, confirming that the nanoparticles themselves did not introduce microbial contamination during the adsorption experiments.

Following the adsorption assays, the nanoparticle-containing fraction was homogenized by vortex mixing in a small volume of sterile physiological saline solution and plated on LB agar to detect bacterial cells associated with the magnetic nanoparticles. Afterwards, the reuse of magnetic nanoparticles was carried out to assess the reusability of the adsorbent—an essential factor from both cost-efficiency and environmental perspectives. The recovery procedure was performed by completely removing the supernatant fraction from the ferrites after the adsorption experiment, and the nanoparticles were placed in a drying oven at 120 °C for 2 h. This temperature far exceeds the survival threshold of *E. coli*, ensuring the complete elimination of the captured bacterial cells. Following this thermal treatment, the sterile nanoparticles were resuspended in 900 µL of physiological saline, and the adsorption experiment was subsequently repeated.

Conclusions

In this study, amine-functionalized $CoFe_2O_4$ nanoparticles were successfully synthesized and demonstrated markedly improved structural, magnetic, and adsorption properties compared to their non-functionalized counterparts.

The functionalization process resulted in the formation of porous spherical aggregates composed of small crystallites, leading to significantly increased surface area and pore volume, as confirmed by both N_2 and CO_2 adsorption measurements. These structural features, together with the presence of surface amine groups, contributed to substantially enhanced adsorption capacities toward Pb(II), Cd(II), and Ni(II) ions, with Pb(II) showing the most favorable uptake behavior. The adsorption performance correlated well with Langmuir-type monolayer adsorption behavior for lead, highlighting the strong interaction between Pb(II) ions and amine-functionalized surfaces. In multicomponent systems, lead removal remained dominant. The adsorption experiments demonstrate that the amine-functionalized $CoFe_2O_4$ developed in this study performs competitively with previously reported ferrite-based adsorbents (Table 3). Surface functionalization clearly enhanced the adsorption efficiency relative to the non-functionalized material, yielding capacities comparable to several graphene- or composite-modified systems, although some literature reports higher maximum values under optimized conditions.

Additionally, the amine-functionalized nanoparticles exhibited highly efficient *E. coli* adsorption performance, achieving complete removal of bacterial cells under the applied experimental conditions and maintaining adsorption efficiency over multiple reuse cycles. While direct comparison with published data (Table 4) is somewhat limited owing to variations in initial cell concentrations and adsorbent dosages, the performance of the present material can be regarded as highly effective among ferrite-based bacterial adsorption systems for low-density *E. coli* suspensions.

Mechanistic evaluation suggested that Pb(II) adsorption was primarily associated with coordination interactions involving surface amine groups, whereas bacterial removal was predominantly governed by electrostatic attraction between protonated amine functionalities and negatively charged bacterial cell-envelope components.

These results demonstrate that surface functionalization substantially enhances the multifunctional adsorption capability of ferrite nanoparticles. The amine-functionalized $CoFe_2O_4$ synthesized in this work showed enhanced toxic metal ion and bacterial adsorption performance, supporting the applicability of such materials for adsorption-assisted removal process in aqueous systems under the investigated experimental conditions. Future studies will focus on evaluating the performance of the material in more complex water matrices and against a broader range of microbial contaminants.

Supplementary Information The online version contains supplementary material available at https://doi.org/10.1038/s41598-026-72024-w.

Acknowledgements Acknowledgement: S.E. supported by the University Research Scholarship Program of the Ministry for Culture and Innovation from the source of the National Research, Development and Innovation Fund. L.V. supported by the János Bolyai Research Scholarship of the Hungarian Academy of Sciences.

Author contributions Conceptualization, E.S., E. Sz-D., L.V.; methodology Á.M.I., D.T., O.A.; formal analysis, F.K., L.D., ; resources, B.V.; data curation, D.T., E.Sz.-D., L.V.; writing—original draft preparation, D. T., O.A., L.V.; writing—review and editing, S.E., E. Sz-D. B.V.; visualization and supervision, E.S., E. Sz-D., L.V.

Funding This research did not receive funding.

Data availability Data is available upon request from the corresponding authors.

Declarations

Competing interests The authors declare no competing interests.

References

1. Duffus, J. H. Heavy metals'—A meaningless term? (IUPAC technical report). *Pure Appl. Chem.* **74**, 793–807 (2002).
2. Hübner, R., Astin, K. B. & Herbert, R. J. H. Heavy metal'--time to move on from semantics to pragmatics? *J. Environ. Monit.* **12**, 1511–1514 (2010).
3. Wang, S., Jiang, S. P. & Wang, X. Microwave-assisted one-pot synthesis of metal/metal oxide nanoparticles on graphene and their electrochemical applications. *Electrochim. Acta*. **56**, 3338–3344 (2011).
4. Mohallem, N. D. S., Silva, J. B., Nascimento, G. L. T. & Guimarães, V. L. Study of multifunctional nanocomposites formed by cobalt ferrite dispersed in a silica matrix prepared by ssol–gell process. In *Nanocomposites—New Trends and Developments* (InTech, 2012). https://doi.org/10.5772/51154. (2012).
5. Kharisov, B. I., Dias, H. V. R. & Kharissova, O. V. Mini-review: Ferrite nanoparticles in the catalysis. *Arab. J. Chem.* **12**, 1234–1246 (2019).
6. Vinosha, P. A. et al. Review on recent advances of synthesis, magnetic properties, and water treatment applications of cobalt ferrite nanoparticles and nanocomposites. *J. Supercond Nov Magn.* **34**, 995–1018 (2021).
7. Jauhar, S., Kaur, J., Goyal, A. & Singhal, S. Tuning the properties of cobalt ferrite: A road towards diverse applications. *RSC Adv.* **6**, 97694–97719 (2016).
8. Behura, R., Sakthivel, R. & Das, N. Synthesis of cobalt ferrite nanoparticles from waste iron ore tailings and spent lithium ion batteries for photo/sono-catalytic degradation of Congo red. *Powder Technol.* **386**, 519–527 (2021).
9. Sharopov, U. et al. Comparative study of cobalt ferrite nanoparticles synthesized by solar and conventional methods. *J. Alloys Compd.* **1043**, 184240 (2025).
10. Thakur, P. et al. Cobalt nanoferrites: A review on synthesis, characterization, and applications. *J. Supercond. Novel Magn.* **35**, 2639–2669 (2022).
11. Lin, Q. et al. Magnetic and Mössbauer spectroscopy studies of zinc-substituted cobalt ferrites prepared by the ssol–gell method. *Materials* **11**, 1799 (2018).
12. Ivanets, A. I. et al. Magnesium ferrite nanoparticles as a magnetic sorbent for the removal of Mn^{2+}, Co^{2+}, Ni^{2+} and Cu^{2+} from aqueous solution. *Ceram. Int.* **44**, 9097–9104 (2018).
13. Joseph, L., Jun, B. M., Flora, J. R. V., Park, C. M. & Yoon, Y. Removal of heavy metals from water sources in the developing world using low-cost materials: A review. *Chemosphere* **229**, 142–159 (2019).
14. Irfan, M. et al. Kinetics and adsorption isotherms of amine-functionalized magnesium ferrite produced using ssol–gell method for treatment of heavy metals in wastewater. *Materials* **15**, 4009 (2022).
15. Al Yaqoob, K., Bououdina, M., Akhter, M. S., Najar, A., Vijaya, J. J. & B. & Selectivity and efficient Pb and Cd ions removal by magnetic MFe_2O_4 (M = Co, Ni, Cu and Zn) nanoparticles. *Mater. Chem. Phys.* **232**, 254–264 (2019).
16. Karcioğlu Karakaş, Z., Boncukcuoğlu, R. & Karakaş, İ. H. Adsorptive properties of As(III) from aqueous solution using magnetic nickel ferrite ($NiFe_2O_4$) nanoparticles: Isotherm and kinetic studies. *Sep. Sci. Technol.* **52**, 21–34 (2017).
17. Kraus, A., Jainae, K., Unob, F. & Sukpirom, N. Synthesis of MPTS-modified cobalt ferrite nanoparticles and their adsorption properties in relation to Au(III). *J. Colloid Interface Sci.* **338**, 359–365 (2009).
18. Asadi, R., Abdollahi, H., Gharabaghi, M. & Boroumand, Z. Effective removal of Zn (II) ions from aqueous solution by the magnetic $MnFe_2O_4$ and $CoFe_2O_4$ spinel ferrite nanoparticles with focuses on synthesis, characterization, adsorption, and desorption. *Adv. Powder Technol.* **31**, 1480–1489 (2020).
19. Asri, N. S., Nurdila, F. A., Kato, T., Iwata, S. & Suharyadi, E. Removal study of Cu(II), Fe(II) and Ni(II) ions from wastewater using polymer-coated cobalt ferrite ($CoFe_2O_4$) magnetic nanoparticles adsorbent. *J. Phys. Conf. Ser.* **1091**, 012016 (2018).
20. Paris, E. C. et al. Faujasite zeolite decorated with cobalt ferrite nanoparticles for improving removal and reuse in Pb2 + ions adsorption. *Chin. J. Chem. Eng.* **28**, 1884–1890 (2020).
21. Saleem, M. U. et al. Study of kinetics and the working mechanism of silica-coated amino-functionalized $CoFe_2O_4$ ferrite nanoparticles to treat wastewater for heavy metals. *ACS Omega*. **56**, 3338–3344 (2024).
22. Khoso, W. A., Haleem, N., Baig, M. A. & Jamal, Y. Synthesis, characterization and heavy metal removal efficiency of nickel ferrite nanoparticles (NFN's). *Sci. Rep.* **11**, 3790 (2021).

23. Iqbal, Z., Tanweer, M. S. & Alam, M. Reduced graphene oxide-modified spinel cobalt ferrite nanocomposite: Synthesis, characterization, and its superior adsorption performance for dyes and heavy metals. *ACS Omega*. **8**, 6376–6390 (2023).
24. Ahmed, M. A., Ahmed, M. A. & Mohamed, A. A. Facile adsorptive removal of dyes and heavy metals from wastewaters using magnetic nanocomposite of zinc ferrite@reduced graphene oxide. *Inorg. Chem. Commun.* **144**, 109912 (2022).
25. Ramadan, R. & El-Masry, M. M. Effect of (Co and Zn) doping on structural, characterization and the heavy metal removal efficiency of $CuFe_2O_4$ nanoparticles. *J. Aust. Ceram. Soc.* **60**, 509–524 (2024).
26. Jayalakshmi, R., Jeyanthi, J. & Aswin Sidhaarth, K. R. Versatile application of cobalt ferrite nanoparticles for the removal of heavy metals and dyes from aqueous solution. *Environ. Nanotechnol. Monit. Manag*. **17**, 100659 (2022).
27. Zhao, X. et al. Synthesis and characterization of gadolinium doped cobalt ferrite nanoparticles with enhanced adsorption capability for Congo Red. *Chem. Eng. J.* **250**, 164–174 (2014).
28. Ding, Z., Wang, W., Zhang, Y., Li, F. & Liu, J. P. Synthesis, characterization and adsorption capability for Congo red of $CoFe_2O_4$ ferrite nanoparticles. *J. Alloys Compd.* **640**, 362–370 (2015).
29. Huang, Y. F., Wang, Y. F. & Yan, X. P. Amine-functionalized magnetic nanoparticles for rapid capture and removal of bacterial pathogens. *Environ. Sci. Technol.* **44**, 7908–7913 (2010).
30. Bohara, R. A., Throat, N. D., Mulla, N. A. & Pawar, S. H. Surface-modified cobalt ferrite nanoparticles for rapid capture, detection, and removal of pathogens: A potential material for water purification. *Appl. Biochem. Biotechnol.* **182**, 598–608 (2017).
31. Franco, A. J. & Alocilja, E. Adsorption studies of salmonella enteritidis and *Escherichia coli* on chitosan-coated magnetic nanoparticles. *Cells* **14**, 225 (2025).
32. Thommes, M. et al. Physisorption of gases, with special reference to the evaluation of surface area and pore size distribution (IUPAC Technical Report). *Pure Appl. Chem.* **87**, 1051–1069 (2015).
33. Wang, H., Su, W. & Tan, M. Endogenous fluorescence carbon dots derived from food items. *Innovation* **1**, 100009 (2020).
34. Zhou, B. et al. Rare-earth-mediated magnetism and magneto-optical Kerr effects in nanocrystalline $CoFeMn_{0.9}RE_{0.1}O_4$ thin films. *J. Magn. Magn. Mater.* **280**, 327–333 (2004).
35. Kurian, M. et al. Structural, magnetic, and acidic properties of cobalt ferrite nanoparticles synthesised by wet chemical methods. *J. Adv. Ceram.* **4**, 199–205 (2015).
36. George, T., Sunny, A. T. & Varghese, T. Magnetic properties of cobalt ferrite nanoparticles synthesized by ssol–gell method. *IOP Conf. Ser. Mater. Sci. Eng.* **73**, 012050 (2015).
37. Xavier, B & Labarta, A. Finite-size effects in fine particles: Magnetic and transport properties. *J. Phys. D Appl. Phys.* **35**, 201 (2002).
38. Alkadir, O. K. A., Al-Mashhadani, Z. I., Aljeboree, A. M. & Alkaim, A. F. Comparison between pseudo-first-order and pseudo-second-order of linear and nonlinear equations adsorption kinetic models for the removal of amoxicillin (AMX) onto hydrogel. *Int. J. Pharm. Qual. Assur.* **12**, 346–350 (2021).
39. Ho, Y. S. & McKay, G. Pseudo-second order model for sorption processes. *Process Biochem.* **34**, 451–465 (1999).
40. Ezzati, R. A new insight into the pseudo-second-order model and the physical meaning of its rate constant in adsorption. *J. Dispers Sci. Technol.* **46**, 222–229 (2025).
41. Guo, T. et al. Mechanism of Cd(II) and Cu(II) adsorption onto few-layered magnetic graphene oxide as an efficient adsorbent. *ACS Omega*. **6**, 16535–16545 (2021).
42. Ungureanu, G., Bejenari, I., Hristea, G. & Volf, I. Carbonaceous materials from forest waste conversion and their corresponding hazardous pollutants remediation performance. *Forests* **13**, 2080 (2022).
43. Duan, S. et al. Effective removal of Pb(II) using magnetic $Co_{0.6}Fe_{2.4}O_4$ micro-particles as the adsorbent: Synthesis and study on the kinetic and thermodynamic behaviors for its adsorption. *Colloids Surf. Physicochem Eng. Asp*. **469**, 211–223 (2015).
44. Abdel Rahman, E. M., El-Subruiti, G. M., Atta, E. R. & Moustafa, A. H. E. Removal of copper and nickel ions from aqueous solution by adsorption on nanobentonite: equilibrium, kinetics, and thermodynamics. *ACS Omega*. **10**, 32680–32690 (2025).
45. Zhang, B. L. et al. Mechanism study about the adsorption of Pb(II) and Cd(II) with iron-trimesic metal-organic frameworks. *Chem. Eng. J.* **385**, 123507 (2020).
46. Hui Ying, N. & Yeong, Y. F. Heavy metal ions removal using amine-functionalized mesoporous adsorbents. *Appl. Mech. Mater.* **625**, 65–68 (2014).
47. Nonkumwong, J., Ananta, S. & Srisombat, L. Effective removal of lead(<scp>ii) from wastewater by amine-functionalized magnesium ferrite nanoparticles. *RSC Adv.* **6**, 47382–47393 (2016).
48. Guo, C., Wang, Y., Wang, F. & Wang, Y. Adsorption performance of amino functionalized magnetic molecular sieve adsorbent for effective removal of lead ion from aqueous solution. *Nanomaterials* **11**, 2353 (2021).
49. Zhang, B. L. et al. Mechanism study about the adsorption of Pb(II) and Cd(II) with iron-trimesic metal-organic frameworks. *Chem. Eng. J.* **385**, 123507 (2020).
50. Godwin, J. et al. Nanosorbent based on coprecipitation of ZnO in goethite for competitive sorption of Cd(II)–Pb(II) and Cd(II)–Pb(II)–Ni(II) systems. *J. Environ. Health Sci. Eng.* **22**, 149–165 (2024).

51. Yang, M., Dang, S., Gao, L. & Zhang, J. Dual-functional amino-carboxyl co-modified Fe_3O_4 nanoparticles for synergistic selective adsorption of lead and cadmium ions from aqueous solutions. *Sci. Rep.* **16**, 7676 (2026).
52. Kaur, M., Kaur, M., Singh, D., Feng, M. & Sharma, V. K. Magnesium ferrite-nitrogen-doped graphene oxide nanocomposite: effective adsorptive removal of lead(II) and arsenic(III) (1931). https://doi.org/10.1007/s11356-022-19314-8.
53. Ilosvai, Á. M. et al. Core–shell structured silver-ferrite nanoparticles for antibacterial action and magnetic removal of bacteria from aqueous media. *Sci. Rep.* **16**, 3582 (2025).
54. Khizar, S. et al. Aminodextran coated $CoFe_2O_4$ nanoparticles for combined magnetic resonance imaging and hyperthermia. *Nanomaterials*. **10**, 2182 (2020).
55. Zheng, S. et al. Implication of surface properties, bacterial motility, and hydrodynamic conditions on bacterial surface sensing and their initial adhesion. *Front. Bioeng. Biotechnol.* **9**, 643722 (2021).
56. Silhavy, T. J., Kahne, D. & Walker, S. The bacterial cell envelope. *Cold Spring Harb Perspect. Biol.* **2**, a000414 (2010).
57. Ito, A., Jitsunobu, H., Kawabe, Y., Ijima, H. & Kamihira, M. Magnetic separation of cells in coculture systems using magnetite cationic liposomes. *Tissue Eng. Part. C Methods*. **15**, 413–423 (2009).
58. Chandler, A. M. et al. Separating pathogens from drinking water and food using magnetic nanomaterials: Opportunities and challenges. *J. Nanobiotechnol.*. https://doi.org/10.1186/S12951-026-04175-X (2026).
59. Franco, D., Calabrese, G., Guglielmino, S. P. P. & Conoci, S. Metal-based nanoparticles: Antibacterial mechanisms and biomedical application. *Microorganisms*. **10**, 1778 (2022).
60. Raji, Z., Karim, A., Karam, A. & Khalloufi, S. Adsorption of heavy metals: Mechanisms, kinetics, and applications of various adsorbents in wastewater remediation—a review. *Waste* **1**, 775–805 (2023).
61. Plazinski, W., Dziuba, J. & Rudzinski, W. Modeling of sorption kinetics: The pseudo-second order equation and the sorbate intraparticle diffusivity. *Adsorption* **19**, 1055–1064 (2013).
62. Lima, É. C., Adebayo, M. A. & Machado, F. M. Kinetic and equilibrium models of adsorption. *Carbon Nanostruct.* **0**, 33–69 (2015).
63. Kumar, K. V. Comments on Adsorption of acid dye onto organobentonite. *J. Hazard. Mater.* **137**, 638–639 (2006).
64. Guo, T. et al. Mechanism of Cd(II) and Cu(II) adsorption onto few-layered magnetic graphene oxide as an efficient adsorbent. *ACS Omega*. https://doi.org/10.1021/ACSOMEGA.1C01770 (2021).
65. Mahmud, M. et al. Co-precipitation synthesis of non-cytotoxic and magnetic cobalt ferrite nanoparticles for purging heavy metal from the aqueous medium: Pb(II) adsorption isotherms and kinetics study. *Chem. Ecol.* **38**, 544–563 (2022).
66. Tran, C. V., Quang, D. V., Nguyen Thi, H. P., Truong, T. N. & La, D. D. Effective removal of Pb(II) from aqueous media by a new design of Cu–Mg binary ferrite. *ACS Omega*. **5**, 7298 (2020).
67. Viltužnik, B., Košak, A., Zub, Y. L. & Lobnik, A. Removal of Pb(II) ions from aqueous systems using thiol-functionalized cobalt-ferrite magnetic nanoparticles. *J. Solgel Sci. Technol.* **68**, 365–373 (2013).
68. He, D. et al. Digestion liquid based alkaline pretreatment of waste activated sludge promotes methane production from anaerobic digestion. *Water Res* **199** (2021).
69. Zaini, M. A. A., Amano, Y. & Machida, M. Adsorption of heavy metals onto activated carbons derived from polyacrylonitrile fiber. *J. Hazard. Mater.* **180**, 552–560 (2010).
70. Brown, G. E. et al. Metal oxide surfaces and their interactions with aqueous solutions and microbial organisms. *Chem. Rev.* **99**, 77–174 (1998).
71. Wang, J., Ma, W. & Wang, X. Insights into the structure of *Escherichia coli* outer membrane as the target for engineering microbial cell factories. *Microbial Cell Factories* **20**, 73 (2021).
72. Nguyen, K. D., Tran, K. D., Le, H. V., Pham, V. T. T. & Ho, P. H. Enhanced fenton-photocatalytic degradation of rhodamine B over cobalt ferrite nanoparticles synthesized by a polyvinylpyrrolidone-assisted grinding method. *Inorg. Chem.* **63**, 23586–23600 (2024).
73. Yahya, M. D., Obayomi, K. S., Abdulkadir, M. B., Iyaka, Y. A. & Olugbenga, A. G. Characterization of cobalt ferrite-supported activated carbon for removal of chromium and lead ions from tannery wastewater via adsorption equilibrium. *Water Sci. Eng.* **13**, 202–213 (2020).
74. Syed, S. S. et al. Adsorption of heavy metal ions and organic pollutants from refining wastewater by magnetically synthesized silver nanoparticles coated with graphene oxide. *Sci. Rep.* **16**, 7681 (2026).
75. Oladimeji, T. et al. Removal of heavy metals from foundry wastewater using magnetic graphene oxide. *Open. Chem. Eng. J.* **20** (2026).
76. Almomani, F., Bhosale, R., Khraisheh, M., kumar, A. & Almomani, T. Heavy metal ions removal from industrial wastewater using magnetic nanoparticles (MNP). *Appl. Surf. Sci.* **506**, 144924 (2020).
77. Abdelmegeed, A. F. et al. Synthesis of functionalized superparamagnetic nanoparticles as highly efficient nanoadsorbents: Removal of heavy metals from industrial wastewater sample as a case study. *Inorg. Chem. Commun.* **155**, 111094 (2023).
78. Souiyah, M. et al. Specific surface area characterization of spinel ferrite nanostructure based compounds for photocatalysis and other applications using extreme learning machine method. *Math. Probl. Eng.* 1–11 (2022).
79. Matouq, M., Jildeh, N., Qtaishat, M., Hindiyeh, M. & Al Syouf, M. Q. The adsorption kinetics and modeling for heavy metals removal from wastewater by Moringa pods. *J. Environ. Chem. Eng.* **3**, 775–784 (2015).

80. Nguyen, K. T. et al. Advances in As contamination and adsorption in soil for effective management. *J. Environ. Manag.* **296**, 113274 (2021).
81. Pinto, M. et al. Application of magnetic nanoparticles for water purification. *Environ. Adv.* **2**, 100010 (2020).
82. Li, Z., Ma, J., Ruan, J. & Zhuang, X. Using positively charged magnetic nanoparticles to capture bacteria at ultralow concentration. *Nanoscale Res. Lett.* **14**, 195 (2019).

Authors and Affiliations

Dóra Tergalecz[1,4] · Orsolya Alberti[1,4] · Maria Ilosvai[1,4] · Ferenc Kristály[2] · Lajos Daróczi[3] · Béla Viskolcz[1,4] · Emma Szőri-Dorogházi[1] · László Vanyorek[1] · Emőke Sikora[1]

✉ Emőke Sikora
emoke.sikora@uni-miskolc.hu

[1] Institute of Chemistry, University of Miskolc, Miskolc 3515, Hungary

[2] Institute of Mineralogy and Geology, University of Miskolc, Miskolc 3515, Hungary

[3] Department of Solid State Physics, University of Debrecen, Debrecen 4010, Hungary

[4] Advanced Materials and Intelligent Technologies Higher Education and Industrial Cooperation Centre, University of Miskolc, Miskolc 3515, Hungary